Cell Reports

NMDA Receptor Autoantibodies in Autoimmune Encephalitis Cause a Subunit-Specific Nanoscale Redistribution of NMDA Receptors

Graphical Abstract

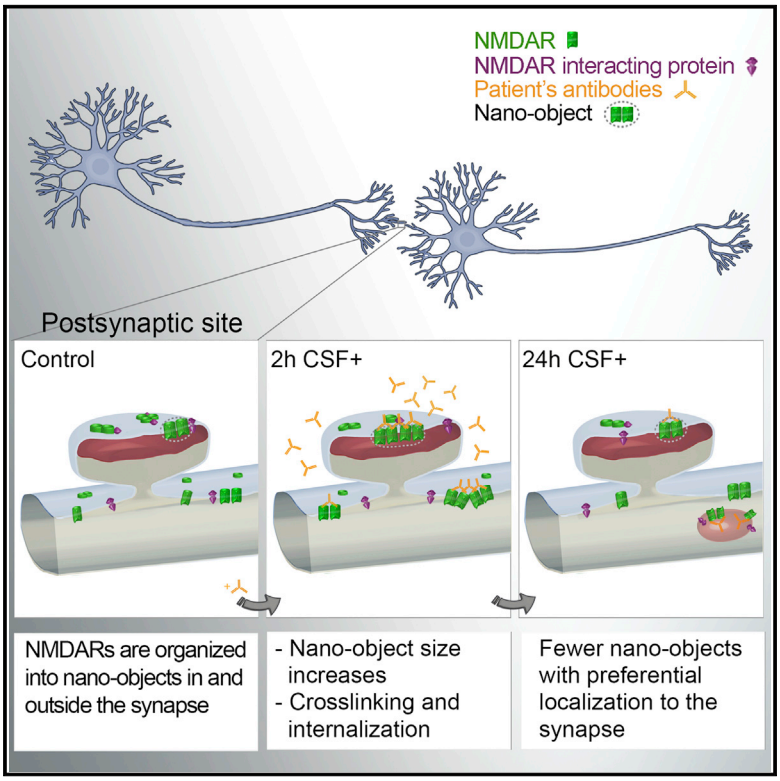

Highlights

- NMDARs form nano-objects on the neuronal surface
- Autoantibodies increase NMDAR nano-object size and content before internalization
- Cross-linking and disruption of NMDAR-protein interactions cause increased clustering
- EphB2 receptor activation antagonizes the antibody effects on NMDAR nano-organization

Authors

Laurent Ladépêche, Jesús Planagumà, Shreyasi Thakur, ..., Lara Laparra-Cuervo, Josep Dalmau, Melike Lakadamyali

Correspondence

laurent.ladepeche@icfo.eu (L.L.), melikel@pennmedicine.upenn.edu (M.L.)

In Brief

Ladépêche et al. visualize NMDAR nano-organization in a model of NMDAR encephalitis. NMDARs organize in nano-objects, which show a time-dependent and subunit-specific change in their size and content upon patients' antibody treatment. EphB2 receptor activation, which stabilizes NMDAR-protein interactions, partially antagonizes the alteration of NMDAR nano-organization caused by patients' antibodies.

Ladépêche et al., 2018, Cell Reports *23*, 3759–3768
June 26, 2018 © 2018 The Authors.
https://doi.org/10.1016/j.celrep.2018.05.096

CellPress

Cell Reports
Report

OPEN ACCESS
CellPress

NMDA Receptor Autoantibodies in Autoimmune Encephalitis Cause a Subunit-Specific Nanoscale Redistribution of NMDA Receptors

Laurent Ladépêche,[1,2,9,*] Jesús Planagumà,[1,2,9] Shreyasi Thakur,[1,5] Irina Suárez,[1,7] Makoto Hara,[2,8] Joseph Steven Borbely,[1] Angel Sandoval,[1] Lara Laparra-Cuervo,[1] Josep Dalmau,[2,3,4,6,10] and Melike Lakadamyali[1,5,10,11,*]
[1]ICFO-Institut de Ciències Fotòniques, The Barcelona Institute of Science and Technology, 08860 Castelldefels (Barcelona), Spain
[2]Institut d'Investigacions Biomèdiques August Pi i Sunyer (IDIBAPS), Hospital Clínic c/ Villarroel 170, 08036 Barcelona, Spain
[3]Department of Neurology, University of Pennsylvania, Philadelphia, PA 19104, USA
[4]Catalan Institution for Research and Advanced Studies (ICREA), 08010 Barcelona, Spain
[5]Department of Physiology, Perelman School of Medicine, University of Pennsylvania, 700 Clinical Research Building, 415 Curie Boulevard, Philadelphia, PA 19104-6085, USA
[6]Centro de Investigación Biomédica en Red de Enfermedades Raras (CIBERER), Av. Monforte de Lemos, 3-5. Pabellón 11. Planta 0, 28029 Madrid, Spain
[7]Present address: Institute for Cardiovascular Organogenesis and Regeneration, Faculty of Medicine, WWU Münster, 48149 Münster, Germany
[8]Present address: Division of Neurology, Department of Medicine, Nihon University School of Medicine, Tokyo, Japan
[9]These authors contributed equally
[10]Senior author
[11]Lead Contact
*Correspondence: laurent.ladepeche@icfo.eu (L.L.), melikel@pennmedicine.upenn.edu (M.L.)
https://doi.org/10.1016/j.celrep.2018.05.096

SUMMARY

Anti-N-methyl-D-aspartate receptor (NMDAR) encephalitis is a severe neuropsychiatric disorder mediated by autoantibodies against the GluN1 subunit of the NMDAR. Patients' antibodies cause cross-linking and internalization of NMDAR, but the synaptic events leading to depletion of NMDAR are poorly understood. Using super-resolution microscopy, we studied the effects of the autoantibodies on the nanoscale distribution of NMDAR in cultured neurons. Our findings show that, under control conditions, NMDARs form nanosized objects and patients' antibodies increase the clustering of synaptic and extrasynaptic receptors inside the nano-objects. This clustering is subunit specific and predominantly affects GluN2B-NMDARs. Following internalization, the remaining surface NMDARs return to control clustering levels but are preferentially retained at the synapse. Monte Carlo simulations using a model in which antibodies induce NMDAR cross-linking and disruption of interactions with other proteins recapitulated these results. Finally, activation of EphB2 receptor partially antagonized the antibody-mediated disorganization of the nanoscale surface distribution of NMDARs.

INTRODUCTION

The N-methyl-D-aspartate receptors (NMDARs) play a critical role in neuronal synaptic plasticity, a cellular correlate for learning and memory processes. NMDARs are heterotetramers mainly comprising two obligatory GluN1 subunits and two GluN2 subunits, of which GluN2A and GluN2B are the main subunits present in the hippocampus (Paoletti, 2011). Anti-NMDAR encephalitis is a recently identified autoimmune synaptopathy characterized by changes in behavior, psychosis, decrease of memory, seizures, stereotyped movements, autonomic instability, and coma (Dalmau and Graus, 2018). These symptoms are accompanied by the presence of autoantibodies in cerebrospinal fluid (CSF) and serum against extracellular epitopes of the GluN1 subunit of the NMDAR (Gleichman et al., 2012).

In cultured neurons and in an animal model of cerebroventricular transfer of patients' CSF, the autoantibodies altered the cell-surface dynamics of the NMDAR, causing their internalization, and decreased the NMDAR-dependent currents and synaptic plasticity, resulting in memory and behavioral alterations (Hughes et al., 2010; Mikasova et al., 2012; Moscato et al., 2014; Planagumà et al., 2015). In these studies, treatment with patients' antibodies caused a disruption of normal surface diffusion of the NMDAR, followed by their internalization. In contrast to these prominent effects on NMDARs, patients' antibodies did not alter the localization or expression of other glutamate receptors or synaptic proteins, number of synapses, dendritic spines, dendritic complexity, or cell survival (Hughes et al., 2010). Moreover, removal of patients' antibodies led to recovery of NMDAR levels, synaptic function, memory, and behavior. Other studies showed that activation of Ephrin-B2 (EphB2) receptor partially antagonized all pathogenic effects of patients' autoantibodies (Mikasova et al., 2012; Planagumà et al., 2016). Yet the time course of the changes of NMDAR distribution that take place at the synaptic level is unknown. Studies have shown that the nanoscale distribution and mobility of synaptic receptors, including NMDARs, are critical for normal neurotransmission

This is an open access article under the CC BY-NC-ND license (http://creativecommons.org/licenses/by-nc-nd/4.0/).

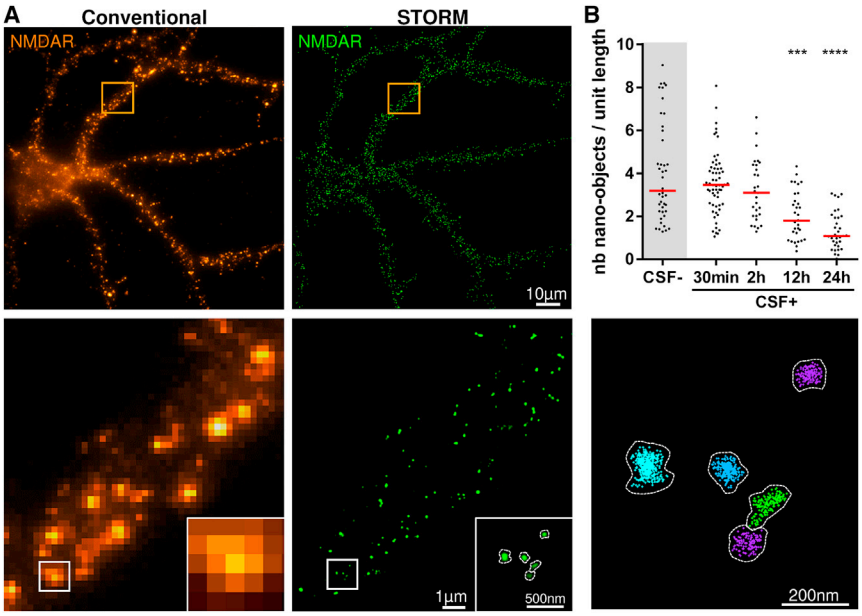

Figure 1. NMDAR Autoantibodies Lead to a Decrease in the Surface Density of NMDAR Nano-objects as Revealed by Super-resolution Microscopy

(A) A representative conventional wide-field (upper left panel) and super-resolution (upper right panel) fluorescence image of NMDAR in cultured hippocampal neurons. Zoom of the region inside the orange square in the conventional image is shown in the lower left panel. A super-resolution image of the region inside the white square is shown in the lower middle panel. The lower right panel displays the result of the cluster analysis, in which each NMDAR nano-object in the super-resolution image is segmented as a different color using the raw localization data. The number of localizations (given by the individual crosses), the area of the nano-objects, and the number of localizations per nano-object can be quantified after cluster analysis.

(B) Neurons were treated for 30 min or 2, 6, 12, or 24 hr with control or patients' CSF (CSF− and CSF+, respectively), and the density of surface NMDAR nano-objects per unit length (in micrometers) of dendrite was measured in the super-resolution images. When compared to control CSF (CSF−), the incubation with patients' CSF (CSF+) caused a significant reduction of the surface NMDAR nano-objects, with a maximal reduction at 24 hr of treatment. Bars represent medians, and dots correspond to individual cells ($n \geq 29$ fields of view; ***$p < 0.001$, ****$p < 0.0001$).
See also Figures S1 and S2.

(Dupuis et al., 2014; MacGillavry et al., 2013; Nair et al., 2013; Pennacchietti et al., 2017; Specht et al., 2013). Therefore, we reasoned that an antibody-mediated disruption of the NMDAR should also alter the nanoscale distribution of these receptors and synaptic function.

In the current study, we used a combination of biochemical approaches, confocal microscopy, super-resolution microscopy, and Monte Carlo simulations to determine the dynamic changes at the nanoscale level that lead to antibody-mediated reduction of surface NMDARs. We show that NMDARs are organized into small clusters or nano-objects inside the synapse and this nanoscale organization of NMDARs is disrupted in a subunit-dependent manner by patients' NMDAR autoantibodies.

RESULTS

Patients' Antibodies Induce Reorganization of Surface NMDAR at the Nanoscale Level

Using cultured hippocampal neurons, we first confirmed that the NMDAR antibodies present in patients' CSF caused internalization of surface NMDARs (Figure S1) (Hughes et al., 2010; Moscato et al., 2014). To determine the events that take place at the synapse leading to this decrease of surface NMDAR levels, we used single-molecule localization microscopy, in particular stochastic optical reconstruction microscopy (STORM) (Oddone et al., 2014; Rust et al., 2006). STORM revealed that under control conditions (neurons cultured in the presence of CSF without NMDAR antibodies), the NMDARs are organized in nanosized clusters along the dendrite (Figure 1A), which we refer to as nano-objects. Using a previously developed cluster analysis algorithm (Ricci et al., 2015), these nano-objects were automatically segmented, revealing their size and receptor content at the nanoscale level (Figure 1A).

Treatment of living cultured neurons with patients' NMDAR antibodies for different times showed a reduction in the number of surface NMDAR nano-objects per unit length of dendrite, reaching a plateau at 24 hr and displaying overall dynamics similar to those described in studies using confocal microscopy (Figure 1B; Figure S1) (Moscato et al., 2014). To investigate the effect of patients' antibodies on synaptic distribution, size, and receptor content of NMDAR nano-objects, we performed dual-color STORM experiments by co-labeling NMDAR and PSD95, a protein of the postsynaptic density (PSD) known to interact with and stabilize the NMDARs at the synapse (Figure 2A). We measured the nearest-neighbor distances (NNDs) between NMDAR and PSD95 nano-objects, the NMDAR nano-object size, and the number of localizations per NMDAR nano-object, which is proportional to the relative number of receptors inside the nano-objects (Dani et al., 2010). Any NMDAR nano-object that was within 200 nm of PSD95 was considered localized at the synapse, whereas more distant nano-objects were considered extrasynaptic (Figures 2A and 2B). This distance cutoff was selected based on an estimation of the approximate size of the synapse using STORM images of Homer-1c (median Homer-1c width = 200 ± interquartile range [IQR] 141–287 nm, n = 622 synapses). Homer-1c is a synaptic structural reference (Figures S2A and S2B) (Dani et al., 2010) that co-localizes with 82% of PSD95 puncta in confocal images (Figures S2C and S2D). This analysis allowed us to distinguish and separately determine the synaptic and extrasynaptic populations of NMDARs.

Under control conditions, both the number of localizations within a nano-object and the size of the nano-objects were larger

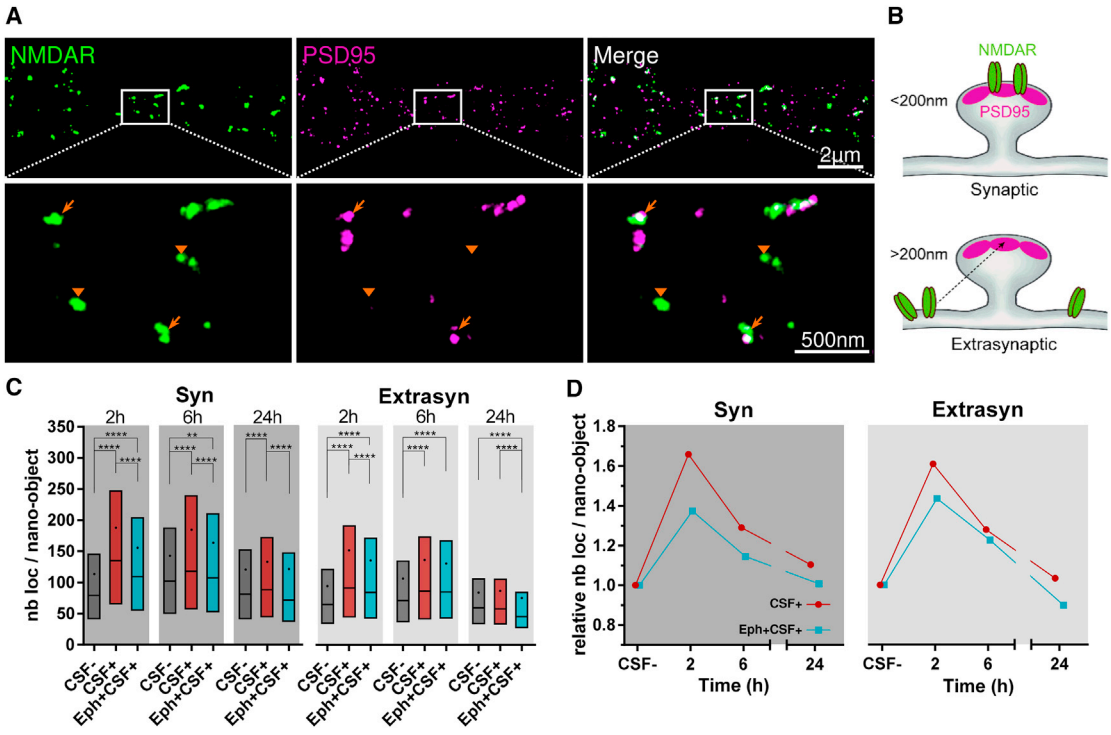

Figure 2. NMDAR Autoantibodies Induce a Time-Dependent Increase in the Receptor Content of the Surface NMDAR Nano-objects

(A) Upper panels show a representative STORM image of the surface NMDAR (green) and PSD95 (magenta). Lower panels are higher magnifications of the white region, showing examples of synaptic (arrows) and extrasynaptic (arrowheads) NMDAR nano-objects.

(B) Schematic illustration representing the distinction used to identify synaptic versus extrasynaptic NMDAR nano-objects located within 200 nm of the center of the closest PSD95 nano-object versus farther away.

(C) Quantification of the number of localizations per NMDAR nano-object, a relative measure of the receptor content of the nano-objects, after 2, 6, or 24 hr of incubation with the control CSF (CSF−, dark gray), with patients' CSF alone (CSF+, red), or in the presence of ephrin-B2 (Eph+CSF+, cyan). The box, line, and dot correspond to interquartile range (IQR, 25th–75th percentile), median, and mean, respectively (synaptic, n ≥ 835 nano-objects; extrasynaptic, n ≥ 2001 nano-objects; **p < 0.01, ***p < 0.001, ****p < 0.0001).

(D) Relative change in the number of localizations per nano-object obtained by normalizing the CSF+ means at each time to the corresponding CSF− means. See also Figure S3.

for those localized in synapses than those localized at extrasynaptic sites (mean number of localizations per nano-object ± SD = 129 ± 133 and 96 ± 95 and mean nano-object size ± SD = 35 ± 12 and 30 ± 10 nm for synaptic, n = 10,720, and extrasynaptic, n = 25,707, respectively) (Figure 2C; Figure S3A). These findings are expected considering the assembly of receptors at the synapse. We observed a slight variability in the nano-object size and the number of receptors per nano-object between control conditions in different experiments (Figure S3C). This variability is likely due to different patients' antibody batches used for labeling (Experimental Procedures) and small differences in the age of the neuronal cultures (17–21 days *in vitro*). Despite the small variability observed, incubation with different batches of patients' antibodies led to a consistent and substantial increase in both the size of the synaptic nano-objects and their relative receptor content starting at 2 hr (Figures 2C and 2D; Figures S3A–S3C). This initial increase was followed by a subsequent decline toward control values for 6–24 hr (Figures 2C and 2D; Figure S3A). The packing density of receptors inside the nano-objects also showed antibody-dependent changes, increasing above control levels (tight packing) at 2 hr and decreasing below control levels (loose packing) at 24 hr (Figure S3B).

Because our protocol involved labeling of NMDAR in live neurons, to ensure that potential secondary antibody cross-linking did not induce artifacts in the NMDAR nano-objects, we performed secondary antibody incubation using either live or fixed neurons to compare the NMDAR nano-object sizes.

Secondary antibodies only slightly increased the size of the NMDAR nano-objects in live neurons (mean nano-object size ± SD: 32 ± 10 nm, n = 4828) compared with fixed neurons (29 ± 9 nm, n = 4791). Therefore, the contribution of secondary antibodies to cross-linking of NMDAR nano-objects is minimal compared with the effects of patients' antibodies. Moreover, this small size change did not affect our findings, because all treatment conditions were equally affected (Figures 2C, 2D, and 3E; Figure S3).

Patients' Antibodies Preferentially Alter the Nanoscale Distribution of GluN2B-Containing Receptors

Previous studies showed that patients' antibodies altered differently the mobility of GluN2A- and GluN2B-containing receptors

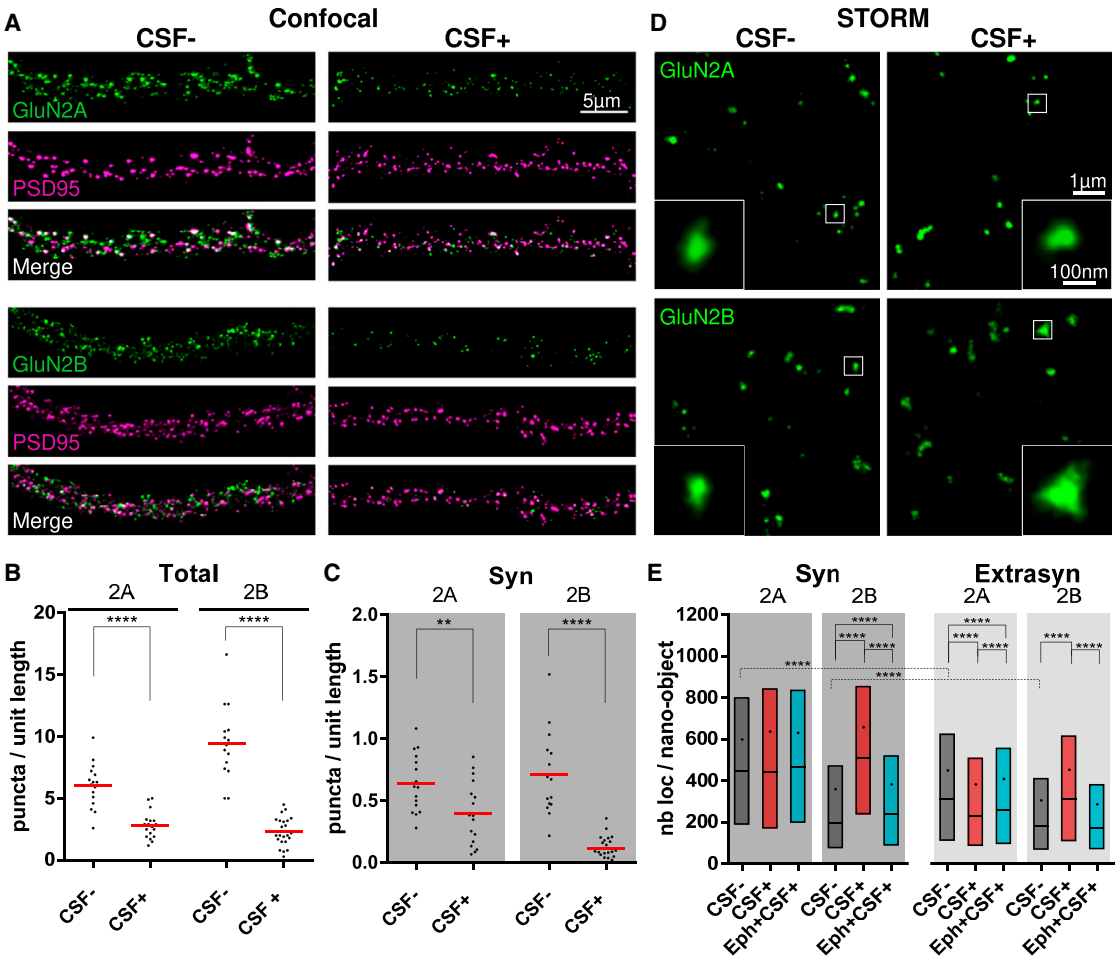

Figure 3. NMDAR Autoantibodies Alter Differently the Distribution of GluN2A-NMDAR and GluN2B-NMDAR

(A) Representative confocal images of surface GluN2A-NMDAR (green, upper panels) or GluN2B-NMDAR (green, lower panels) subunits labeled, together with PSD95 (magenta), after 24 hr of incubation of control or patients' CSF (CSF−, left panels, and CSF+, right panels). Note the visible decrease in the GluN2A and GluN2B labeling in the presence of the patients' CSF.

(B and C) Quantification of the density of surface GluN2A or GluN2B puncta per unit length (in micrometers) of dendrite either considering all surface puncta (B, Total) or isolating the ones that co-localize with PSD95, and are synaptic (C, Syn). Red lines represent the means, and dots correspond to individual cells ($n \geq 15$ fields of view; $^{**}p < 0.01$, $^{***}p < 0.001$, $^{****}p < 0.0001$).

(D) Representative STORM images of GluN2A (upper) and GluN2B (lower) that have been incubated with control or patients' CSF (CSF−, left panels, and CSF+, right panels, respectively) for 24 hr. Insets show zooms of nano-objects corresponding to the white squared region. Note the increased size of the GluN2B nano-objects in the CSF+ condition.

(E) Quantification of the number of localizations per NMDAR nano-object after 24 hr of incubation with control CSF (CSF−, dark gray), with patients' CSF alone (CSF+, red), or in the presence of ephrin-B2 (Eph+CSF+, cyan). The box, line, and dot correspond to IQR, median, and mean, respectively (synaptic, $n \geq 2{,}649$ nano-objects; extrasynaptic, $n \geq 5{,}213$ nano-objects; $^{****}p < 0.0001$).

See also Figures S4 and S5.

(Mikasova et al., 2012). To gain more insight into how NMDARs containing these subunits are organized at the nanoscale level and the effect of patients' antibodies on this organization, we quantified the antibody-mediated changes in the nanoscale distributions of GluN2A- and GluN2B-NMDAR using cultured rodent hippocampal neurons treated with patients' CSF antibodies for 24 hr.

We first assessed the change of cell-surface protein levels of GluN2A and GluN2B using immunoblot of biotinylated cell-surface proteins (Figure S4A). These studies showed a significant decrease of cell-surface GluN1, as well as GluN2A and GluN2B protein levels (Figure S4B). In parallel, we quantified with confocal microscopy the number of GluN2A and GluN2B puncta per unit length of dendrite (Figures 3A–3C). Consistent with western blot findings, there was a decrease in both the total and the synaptic density of NMDARs, regardless of their composition (Figures 3B and 3C). As previously reported using confocal microscopy (Hughes et al., 2010), these changes were not due to synaptic loss, because the density of PSD95 was unaffected (control CSF mean = 8.4 ± 2.3 puncta/unit length, n = 31

dendrites; patients' CSF mean = 7.6 ± 2.3 puncta/unit length, n = 41 dendrites). There was a greater reduction of GluN2B (79% and 87% reduction, $p < 0.0001$ for total and synaptic GluN2B, respectively) compared to GluN2A (55% and 38% reduction, $p < 0.0001$ and $p = 0.0059$ for total and synaptic GluN2A, respectively) (Figures 3A–3C), suggesting a different effect of the antibodies on the NMDAR subpopulations.

We next imaged GluN2A- and GluN2B-NMDAR subpopulations using STORM microscopy. These subunits were also organized in nano-objects, similar to the GluN1 subunit. As expected, both the GluN2A and the GluN2B nano-objects showed substantial co-localization with the obligatory GluN1 subunit (Figures S5A and S5C). This high co-localization was confirmed by NND analysis between GluN2A or GluN2B and GluN1 nano-objects (GluN2A to GluN1 NND median = 50 ± IQR 22–151 nm, n = 5,997; GluN2B to GluN1 NND median = 40 ± IQR 20–97 nm, n = 7,663) (Figures S5B and S5D). Under control conditions, the synaptic GluN2A nano-objects were substantially larger and contained more receptor localizations than their extrasynaptic counterparts (synaptic GluN2A mean number of localizations ± SD = 600 ± 602 localizations, n = 4,912; extrasynaptic GluN2A mean number of localizations ± SD = 451 ± 489 localizations, n = 9,312) (Figure 3E; Figure S5E). In contrast, the GluN2B nano-objects were more similar in size regardless of their localization (synaptic GluN2B mean number of localizations ± SD = 360 ± 462 localizations, n = 4,219; extrasynaptic GluN2B mean number of localizations ± SD = 307 ± 372 localizations, n = 7,938) (Figure 3E; Figure S5E). Furthermore, GluN2A nano-objects were larger overall compared to the GluN2B nano-objects (Figure 3E; Figure S5E). These results are consistent with the preferential occupancy of mature synapses by GluN2A-NMDARs (Flint et al., 1997; Hoffmann et al., 2000; Matta et al., 2011; Paoletti, 2011; Shi et al., 1997; Xing et al., 2006; Zhang and Sun, 2011). Treatment with patients' antibodies increased the size and the receptor content of the GluN2B nano-objects, whereas the size of the GluN2A nano-objects remained similar or slightly decreased compared to control conditions (Figure 3E; Figure S5E). These subunit-specific effects were not due to differences in the patients' CSF used, given that the same CSF was used to determine the effects on each subunit. Overall, these findings show that despite a general reduction of surface NMDAR, the local synaptic reorganization caused by patients' antibodies occurs in a subunit-dependent manner, with the GluN2B subpopulation being preferentially affected. These findings are also in agreement with the greater antibody-induced reduction of GluN2B-NMDARs observed with confocal microscopy.

Treatment with Ephrin-B2 Antagonizes the Antibody-Induced Nanoscale Changes in the Surface Distribution of NMDAR

EphB2 is known to interact with NMDAR (Dalva et al., 2000). Previous studies showed that patients' antibodies disrupt this interaction and that activation of EphB2 by its ligand (ephrin-B2) antagonizes the antibody-induced receptor internalization, preventing the behavioral and memory deficits observed in an animal model of anti-NMDAR encephalitis (Planagumà et al., 2016). In addition, EphB2 activation prevented the antibody-induced alteration of NMDAR surface trafficking (Mikasova et al., 2012). To determine at the nanoscale level the effect of EphB2 activation on antibody-induced NMDAR changes, we used STORM imaging on neurons co-treated with patients' NMDAR antibodies and soluble ephrin-B2. Ephrin-B2 partially prevented the antibody-induced alterations in nano-object size and receptor content for both GluN1 and GluN2B subunits (Figures 2C, 2D, and 3E; Figures S3A, S3B, and S5E). This effect was already evident after 2 hr of co-treatment with patients' antibodies and ephrin-B2 (Figures 2C and 2D). These findings suggest that EphB2 activation prevents antibody-induced NMDAR clustering at the nanoscale level, which likely slows receptor internalization, keeping the surface receptor levels and receptor distribution.

Monte Carlo Simulations Recapitulate the Experimental Findings

To gain insight into the mechanisms behind these experimental observations, we carried out Monte Carlo simulations. Receptors were initially placed randomly in the synapse and extrasynaptic space according to our experimental observations (Experimental Procedures). Pockets of scaffold protein regions (SPRs) were randomly distributed in the synaptic and extrasynaptic surfaces. SPRs were assumed to act as sites of receptor clustering (Figure 4A) due to scaffold protein-receptor binding interactions. Such scaffold nanodomains have been observed in super-resolution images of PSD95 (Nair et al., 2013). The simulations were run for different times (2, 6, and 24 hr), and the surface distribution of receptors was determined at the end point. Receptors that were within 15 nm (roughly the experimental resolution) were considered to belong to a nano-object. The parameters of the simulation were optimized such that the receptors per nano-object remained constant over the different time points of the control simulation (Experimental Procedures; Video S1).

Simulation 1

To capture the receptor dynamics in the presence of patients' NMDAR antibodies, we took into account the occurrence of antibody-induced cross-linking by allowing nano-object formation whenever 2 or more receptors were within 9 nm of one another (approximate diameter of a receptor-antibody complex). Second, we implemented internalization of extrasynaptic nano-objects with a rate determined from the experimental data (Figures S6F–S6H; Supplemental Experimental Procedures). These two effects only partially recapitulated the experimentally observed changes to NMDAR nano-objects in the presence of patients' antibodies (Figures S6B and S6C). With this simulation, the number of NMDARs inside the nano-objects initially increased and then decreased, similar to what was observed in the experiments. However, at 6 hr, there was still significant clustering of synaptic NMDARs above levels observed in the control simulation, contrary to experimental data. In addition, the extrasynaptic clustering was substantially higher than the synaptic clustering, which is opposed to the experimental results. Therefore, antibody-induced cross-linking and internalization alone could not fully capture the experimental results.

Simulation 2

Based on previous reports (Mikasova et al., 2012; Planagumà et al., 2016) and our data showing that activation of EphB2

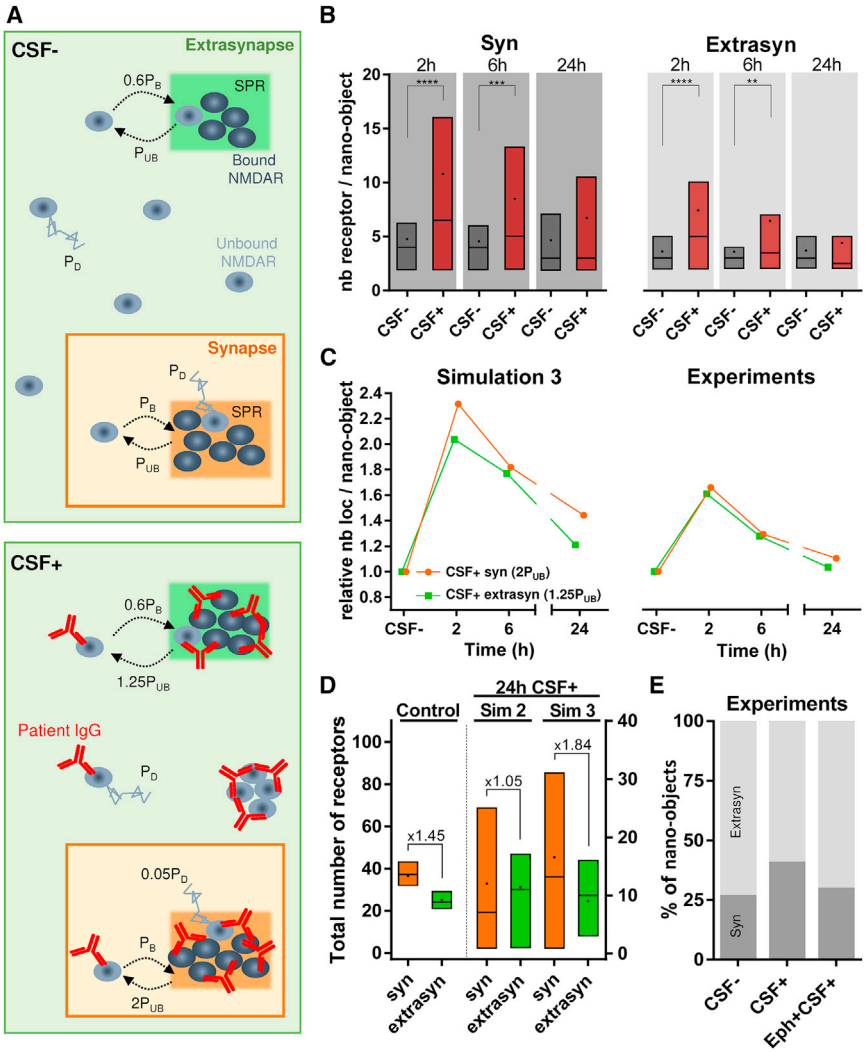

Figure 4. Monte Carlo Simulations Recapitulate Experimental Results

(A) Schematic representation (top view) of NMDAR dynamics simulation for CSF− (control or without antibodies) and CSF+ (with NMDAR antibodies). The synapse and extrasynapse are represented as orange and green areas, respectively (not represented here at their true scale value), with one scaffold protein region (SPR) in each. The receptors follow binding and unbinding events with the scaffold proteins in the SPR and can be in a bound state (dark gray) or an unbound state (light gray). The binding probability of a receptor is $P_B = 1$ in the synapse and $0.6P_B$ in the extrasynapse for both CSF− and CSF+. The unbinding probability of a receptor is $P_{UB} = 0.167$ in both the extrasynapse and the synapse for CSF−. For CSF+, unbinding probability increases to $1.25P_{UB}$ in the extrasynapse and $2P_{UB}$ in the synapse. All unbound receptors diffuse with a probability $P_D = 1$ for CSF−. For CSF+, unbound receptors belonging to a nano-object diffuse with a reduced probability of $0.05P_D$, but this diffusion probability remains unchanged for unbound receptors not forming any nano-object.

(B) Distribution of receptors per nano-object at 2, 6, and 24 hr in the synapse and extrasynapse for both CSF− and CSF+ conditions obtained from simulation. The box, line, and dot correspond to IQR, median, and mean, respectively (synaptic, $n \geq 56$ nano-objects; extrasynaptic, $n \geq 60$ nano-objects; $^{**}p < 0.01$, $^{***}p < 0.001$, $^{****}p < 0.0001$).

(C) Comparison of the fold change in nano-object content at different times (2, 6, and 24 hr) relative to the corresponding CSF− values for simulations (left) and experimental data (right). Each data point is obtained by normalizing the mean of receptors per nano-object value at each time point for CSF+ with the mean of receptors per nano-object value obtained from the corresponding time points for CSF−.

(D) Total number of receptors present in the synapse (orange) and extrasynapse (green) at 24 hr for simulation control (left), simulation 2 (middle), and simulation 3 (right). Data are obtained from the simulated area of ~200 × 200 nm^2 for both synapse and extrasynapse. The fold difference from the mean of the synaptic to the extrasynaptic number of receptors is indicated above the boxes. The box, line, and dot correspond to IQR, median, and mean, respectively (control, n = 40 runs; simulation 2, n = 19 runs; simulation 3, n = 22 runs).

(E) Quantification of percentage of synaptic (dark gray) versus extrasynaptic (light gray) nano-objects from experimental data after 24 hr of treatment with patients' CSF alone (CSF+) or in the presence of ephrin-B2 (Eph+CSF+).

See also Figure S6 and Videos S1, S2, and S3.

antagonizes the effects of the antibodies, we hypothesized that the binding of antibodies to NMDAR leads to a disruption of its interaction with EphB2 and possibly other synaptic interacting partners. We thus increased by two-fold the unbinding rate of synaptic receptors from the SPR to reflect a potential disruption of receptor-protein interactions (Supplemental Experimental Procedures). This modification could recapitulate better the experimental observations at the synaptic level, but the amount of extrasynaptic NMDAR clustering remained inappropriately high compared with that of the synaptic NMDAR clustering (Figures S6D and S6E).

Simulation 3

Based on the preceding results, we hypothesized that interaction with proteins like EphB2 contributes to NMDAR dynamics not only at the synapse but also at the extrasynapse, albeit to a lesser extent, and that these interactions are disrupted by antibody binding. Therefore, we also increased the unbinding rate of extrasynaptic receptors from SPR. Compared with simulations 1 and 2, simulation 3 recapitulated better the experimental data on NMDAR nano-objects (Figure 4B; Videos S2 and S3) both inside and outside of the synapse, suggesting that NMDAR-protein interactions at both the synaptic and the extrasynaptic sites are important for NMDAR dynamics and account for the antibody-induced redistribution of surface NMDARs at the nanoscale level.

Using simulation 3, we also found that upon antibody treatment, more receptors were localized in the synapse compared to control simulation (Figure 4D). To experimentally validate this

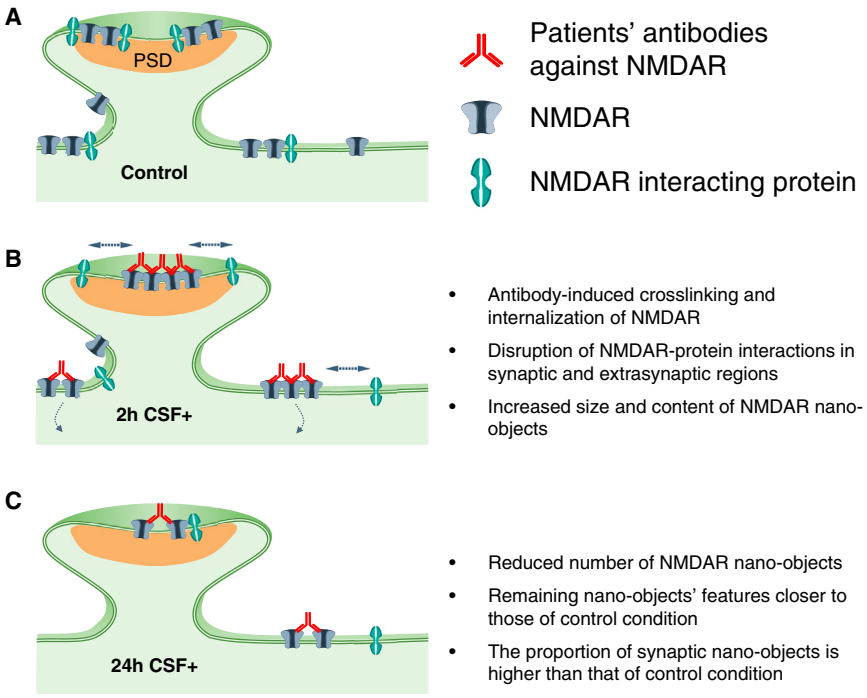

Figure 5. Schematic Representation of the Changes Occurring in NMDAR Organization following Treatment with Patients' NMDAR Antibodies

(A) Under control conditions, NMDAR are distributed at the neuronal surface, forming nano-objects both inside and outside the synapse.

(B) At early times, antibody-induced clustering leads to formation of larger nano-objects containing more receptors, particularly in the synapse.

(C) At later times, dynamic exchange of receptors, facilitated by the disruption of NMDARs' interaction with other proteins in both the synapse and the extrasynapse, coupled with clustering-induced internalization, leads to a decrease in NMDAR nano-object size and content back toward control values while leading to an overall global decrease of NMDAR nano-objects.

result, we quantified the observed percentage of synaptic and extrasynaptic NMDAR nano-objects under control conditions and after 24 hr of antibody treatment. In the analysis of the experimental data, the number of nano-objects was not normalized to the dendrite length. Because the total extrasynaptic length is larger than the synaptic length, the total number of experimentally determined extrasynaptic nano-objects appeared higher than the number of synaptic ones. Nonetheless, this analysis showed that the proportion of synaptic nano-objects increased with antibody treatment compared to control conditions and this effect could be partially antagonized with EphB2 activation (Figure 4E). Along with the total amount of surface NMDAR being significantly lower at this time point, the experimental and simulation results suggest that the remaining population of surface NMDAR is preferentially relocalized at the synapse. A different affinity of the receptors for SPR at the synapse compared with the extrasynaptic site seems to be crucial for this preferential retention of receptors at the synapse.

DISCUSSION

We previously reported that NMDAR antibodies from patients with anti-NMDAR encephalitis cause a decrease of cell-surface and synaptic NMDAR density, as well as total NMDAR protein in cultured hippocampal neurons (Hughes et al., 2010; Moscato et al., 2014). Additional studies showed that patients' antibodies alter the surface trafficking of NMDAR and that this effect is different depending on the GluN2 subunit composition (Mikasova et al., 2012). Here, we used super-resolution microscopy to determine the effect of patients' antibodies on the nanoscale distribution of synaptic and extrasynaptic NMDARs. Our findings show that NMDARs are normally organized into nano-objects, revealed by labeling both the GluN1 and the GluN2 subunits. These nano-objects are larger in the synapse than in the extrasynaptic spaces, and the synaptic GluN2A nano-objects are larger than the GluN2B nano-objects. These findings indicate an organization of the NMDARs at the nanoscale level that is subunit dependent. Such non-uniform enrichment of receptors into nanosized objects and domains has been previously reported for other synaptic proteins such as the AMPAR, for which nano-objects were visualized using both antibody labeling and fluorescent protein fusions (MacGillavry et al., 2013; Nair et al., 2013). In line with the studies on AMPAR, our findings support a model in which surface receptors are compartmentalized within the postsynaptic density, and this compartmentalization likely plays an important role in receptor physiology.

Previous studies using *in vitro* and *in vivo* models demonstrated that patients' CSF antibodies decrease the NMDAR surface and synaptic content and induce severe memory deficits (Hughes et al., 2010; Moscato et al., 2014; Planagumà et al., 2015). Recombinant human monoclonal NMDAR autoantibodies derived from patients' plasma cells had the same effects as those reported for patients' CSF antibodies (Malviya et al., 2017), indicating that the observed effects were caused by the antibodies, not by other CSF factors. Moreover, autoantibody-derived F(ab) (antigen binding) fragments did not decrease surface receptor density (Moscato et al., 2014), indicating that the cross-linking and internalization of NMDAR required the two arms of the antibody molecule and were not due to the labeling procedure. The current findings show that patients' antibodies caused an increased clustering of both synaptic and extrasynaptic NMDARs inside nano-objects, and these changes preceded receptor internalization (Figure 5). This antibody-induced receptor clustering likely triggers internalization once nano-objects reach a threshold size after approximately 2 hr of incubation with patients' antibodies. At later times, the sizes of the remaining surface nano-objects returned to control

values, but the receptors were more loosely packed, having a lower density than those observed in control conditions (Figure 5). We found that antibodies preferentially clustered NMDARs containing GluN2B subunits. Previous studies showed that antibody treatment led to slower diffusion of GluN2B-containing NMDARs (Mikasova et al., 2012), which is consistent with the current super-resolution data in which GluN2B subunits became confined into larger nano-objects after antibody treatment. In the future, it would be interesting to determine the molecular mechanisms leading to subunit-specific reorganization of receptor nano-objects.

Antibody-induced clustering of proteins has been described using conventional microscopy in several pathological conditions (Harder et al., 1998; Mayor et al., 1994; Marta et al., 2005); however, not all autoantibodies to synaptic receptors induce receptor aggregation. For example, in patients with another form of autoimmune encephalitis mediated by GABAb receptor antibodies, the antibodies do not cluster or internalize the cognate receptors (Dalmau et al., 2017). Using super-resolution microscopy, we could visualize the nanoscale organization of receptors and quantify the relative changes to the number of receptors in the nano-objects, which is not possible with conventional microscopy methods.

Monte Carlo simulations showed that NMDAR cross-linking by antibodies was not sufficient to explain the time course of changes affecting the NMDAR nano-objects. Simulations recapitulated the experimental observations taking into account four effects at the molecular level: (1) antibody-induced cross-linking of NMDARs, (2) increased rate of NMDAR internalization following receptor clustering, (3) disruption of NMDAR-protein interactions in the synapse, and (4) disruption of NMDAR-protein interactions at the extrasynaptic space. Consistent with these results, activation of EphB2 by its ligand ephrin-B2 antagonized the antibody-induced alterations of the NMDAR nanoscale distribution in both synaptic and extrasynaptic regions. An interesting prediction of the simulations was the antibody-induced relative increase of the density of synaptic versus extrasynaptic receptors, which was in line with the experimental findings. Our data suggest that differences in the strength of NMDAR-SPR interactions in synaptic and extrasynaptic spaces played an important role in this preferential relocalization of receptors at the synapse. It is likely that the interaction of NMDARs with several synaptic and extrasynaptic partners, in addition to EphB2 receptors, stabilizes NMDAR inside nano-objects and that patients' antibodies disrupt such interactions, explaining why EphB2 activation partially antagonizes the antibody effects. Based on these findings, a task for the future is to determine other interacting partners of NMDAR, the binding of which may also be disrupted by patients' antibodies. Intervention on these binding partners may have therapeutic implications similar to those experimentally demonstrated for EphB2 activation by ephrin-B2-like agonists (Mikasova et al., 2012; Planagumà et al., 2016).

EXPERIMENTAL PROCEDURES

Full details of the experimental procedures and analyses are provided online in the Supplemental Experimental Procedures.

Human CSF Samples and Animal Procedures

Samples of CSF from 5 patients with high-titer NMDAR antibodies (CSF+, determined according to previous studies; see Dalmau et al., 2008) were used on cultured neurons to determine the effects of patients' antibodies (Table S1). Samples of CSF from 5 subjects lacking NMDAR antibodies (CSF−) were used as controls (Table S1). Written consent for studies was obtained from patients or family members. Studies were approved by the institutional review board of Hospital Clínic and Institut d'Investigacions Biomèdiques August Pi i Sunyer (IDIBAPS), Universitat de Barcelona.

Primary hippocampal neurons were prepared from embryonic day (E) 18 embryos extracted from pregnant Wistar rats (Supplemental Experimental Procedures). Animal procedures were conducted in accordance with standard ethical guidelines (European Communities Directive 86/609/EU) and approved by the local ethical committees.

Sample Preparation and STORM Imaging

Primary hippocampal neurons that had been cultured for 17–21 days *in vitro* were treated with either control or patients' CSF for 2, 6, or 24 hr in the presence or absence of ephrin-B2 (0.5 $\mu g.mL^{-1}$). Surface proteins were labeled by incubating live cells for 30 min at 37°C with primary antibodies and then with the corresponding secondary antibodies labeled with the Alexa Fluor 405-Alexa Fluor 647 dye pair for 30 min at 37°C. Synaptic markers were labeled after fixation and permeabilization steps by incubating cells for 1 hr at room temperature (RT) with the corresponding primary antibodies and another 1 hr of incubation at RT with a corresponding secondary antibody prepared for STORM imaging.

All imaging experiments were carried out with a commercial STORM microscope system from Nikon Instruments (NSTORM). For single-color imaging, 647 nm laser light was used for exciting the reporter dye (Alexa Fluor 647, Invitrogen) and switching it to the dark state, and 405 nm laser light was used for reactivating the Alexa Fluor 647 into a fluorescent state in an activator dye (Alexa Fluor 405)-facilitated manner. Dual-color imaging was performed with two sets of secondary antibodies labeled with the same reporter dye (Alexa Fluor 647) but two activator dyes (Alexa Fluor 405 and Cy3) (Bates et al., 2007). The emitted light was collected by an oil immersion 100×, 1.49 numerical aperture (NA) objective; filtered by an emission filter (ET705/72 m); and imaged onto an electron-multiplying charge-coupled device (EMCCD) camera at an exposure time of 20 ms per frame.

STORM Data Analysis

The final images were rendered by representing each x-y position (localization) as a Gaussian with a width that corresponds to the determined localization precision (9 nm). Sample drift during acquisition and crosstalk between the imaging channels were accounted for and corrected (Huang et al., 2008), and a cluster analysis algorithm previously developed in the team (Ricci et al., 2015) was used to group localizations in nano-objects (Supplemental Experimental Procedures). Nano-objects' sizes were calculated as the SD of localization coordinates from the relative nano-object centroid.

Monte Carlo Simulations

Details of the simulations can be found in Supplemental Experimental Procedures.

Statistics

Confocal spot densities of GluN1 and PSD95 were analyzed using one-way ANOVA and post hoc testing with Tukey adjustment for multiple comparisons. Confocal spot densities of GluN2A and GluN2B were analyzed using the t test with Welch's correction. Quantitative immunoblot data were analyzed using the t test with Welch's correction.

STORM nano-object properties, following a non-normal distribution, were analyzed using non-parametric statistics. The Mann-Whitney test was used for pair comparisons, while the Kruskal-Wallis test, followed by post hoc testing with Dunn's correction, was applied for multiple comparisons.

A p value inferior to 0.05 was considered significant. All tests were done using GraphPad Prism v.6 (GraphPad, La Jolla, CA, USA).

SUPPLEMENTAL INFORMATION

Supplemental Information includes Supplemental Experimental Procedures, six figures, one table, and three videos and can be found with this article online at https://doi.org/10.1016/j.celrep.2018.05.096.

ACKNOWLEDGMENTS

We thank all members of the Advanced Fluorescence Imaging and Biophysics group (Institute of Photonic Sciences [ICFO], Barcelona), L. Groc (University of Bordeaux), and A.L. Carvalho (University of Coimbra) for critical reading of the manuscript and helpful discussions. We thank B. Huang (University of California, San Francisco [UCSF]) for Insight3 STORM analysis software. We thank M. Rivas Jiménez (Institute of Photonic Sciences [ICFO], Barcelona) for her technical support with cell cultures. We thank P. Relich (University of Pennsylvania) for his help with the video illustrations. We thank A. Hirschmann (Institute of Photonic Sciences [ICFO], Barcelona) for her help in designing the graphical abstract. We acknowledge the ICFO Super-resolution Light Nanoscopy (SLN) facility and the ICFO Nikon Center of Excellence in STORM. This work was supported by Instituto Carlos III/FEDER PIE 16/00014, CIBERER 15/00010, NIH RO1NS077851, Generalitat de Catalunya AGAUR SGR93, and Fundació CELLEX (M.L. and J.D.); the European Commission's Marie Curie Actions for Co-funding of Regional, National and International Programmes (COFUND); and the Spanish Ministry of Economy and Competitiveness (MINECO) (L.L.).

AUTHOR CONTRIBUTIONS

L.L., J.P., J.D., and M.L. designed the experiments and data analysis. L.L., J.P., I.S., M.H., and L.L.-C. performed the experiments and data analysis. S.T. designed, ran, and analyzed the Monte Carlo simulations. J.S.B. wrote the software for data analysis. A.S. labeled the antibodies for STORM. M.L., L.L., J.P., and J.D. wrote the manuscript. All authors provided feedback on the manuscript. M.L. and J.D. supervised the project.

DECLARATION OF INTERESTS

J.D. holds a patent for the use of Ma2 and NMDAR as an autoantibody test, receives royalties related to this test, and has an unrestricted research grant from Euroimmun.

Received: September 16, 2017
Revised: March 16, 2018
Accepted: May 30, 2018
Published: June 26, 2018

REFERENCES

Bates, M., Huang, B., Dempsey, G.T., and Zhuang, X. (2007). Multicolor super-resolution imaging with photo-switchable fluorescent probes. Science *317*, 1749–1753.

Dalmau, J., and Graus, F. (2018). Antibody-Mediated Encephalitis. N. Engl. J. Med. *378*, 840–851.

Dalmau, J., Gleichman, A.J., Hughes, E.G., Rossi, J.E., Peng, X., Lai, M., Dessain, S.K., Rosenfeld, M.R., Balice-Gordon, R., and Lynch, D.R. (2008). Anti-NMDA-receptor encephalitis: case series and analysis of the effects of antibodies. Lancet Neurol. *7*, 1091–1098.

Dalmau, J., Geis, C., and Graus, F. (2017). Autoantibodies to Synaptic Receptors and Neuronal Cell Surface Proteins in Autoimmune Diseases of the Central Nervous System. Physiol. Rev. *97*, 839–887.

Dalva, M.B., Takasu, M.A., Lin, M.Z., Shamah, S.M., Hu, L., Gale, N.W., and Greenberg, M.E. (2000). EphB receptors interact with NMDA receptors and regulate excitatory synapse formation. Cell *103*, 945–956.

Dani, A., Huang, B., Bergan, J., Dulac, C., and Zhuang, X. (2010). Superresolution imaging of chemical synapses in the brain. Neuron *68*, 843–856.

Dupuis, J.P., Ladépêche, L., Seth, H., Bard, L., Varela, J., Mikasova, L., Bouchet, D., Rogemond, V., Honnorat, J., Hanse, E., and Groc, L. (2014). Surface dynamics of GluN2B-NMDA receptors controls plasticity of maturing glutamate synapses. EMBO J. *33*, 842–861.

Flint, A.C., Maisch, U.S., Weishaupt, J.H., Kriegstein, A.R., and Monyer, H. (1997). NR2A subunit expression shortens NMDA receptor synaptic currents in developing neocortex. J. Neurosci. *17*, 2469–2476.

Gleichman, A.J., Spruce, L.A., Dalmau, J., Seeholzer, S.H., and Lynch, D.R. (2012). Anti-NMDA receptor encephalitis antibody binding is dependent on amino acid identity of a small region within the GluN1 amino terminal domain. J. Neurosci. *32*, 11082–11094.

Harder, T., Scheiffele, P., Verkade, P., and Simons, K. (1998). Lipid domain structure of the plasma membrane revealed by patching of membrane components. J. Cell Biol. *141*, 929–942.

Hoffmann, H., Gremme, T., Hatt, H., and Gottmann, K. (2000). Synaptic activity-dependent developmental regulation of NMDA receptor subunit expression in cultured neocortical neurons. J. Neurochem. *75*, 1590–1599.

Huang, B., Wang, W., Bates, M., and Zhuang, X. (2008). Three-dimensional super-resolution imaging by stochastic optical reconstruction microscopy. Science *319*, 810–813.

Hughes, E.G., Peng, X., Gleichman, A.J., Lai, M., Zhou, L., Tsou, R., Parsons, T.D., Lynch, D.R., Dalmau, J., and Balice-Gordon, R.J. (2010). Cellular and synaptic mechanisms of anti-NMDA receptor encephalitis. J. Neurosci. *30*, 5866–5875.

MacGillavry, H.D., Song, Y., Raghavachari, S., and Blanpied, T.A. (2013). Nanoscale scaffolding domains within the postsynaptic density concentrate synaptic AMPA receptors. Neuron *78*, 615–622.

Malviya, M., Barman, S., Golombeck, K.S., Planagumà, J., Mannara, F., Strutz-Seebohm, N., Wrzos, C., Demir, F., Baksmeier, C., Steckel, J., et al. (2017). NMDAR encephalitis: passive transfer from man to mouse by a recombinant antibody. Ann. Clin. Transl. Neurol. *4*, 768–783.

Marta, C.B., Montano, M.B., Taylor, C.M., Taylor, A.L., Bansal, R., and Pfeiffer, S.E. (2005). Signaling cascades activated upon antibody cross-linking of myelin oligodendrocyte glycoprotein: potential implications for multiple sclerosis. J. Biol. Chem. *280*, 8985–8993.

Matta, J.A., Ashby, M.C., Sanz-Clemente, A., Roche, K.W., and Isaac, J.T.R. (2011). mGluR5 and NMDA receptors drive the experience- and activity-dependent NMDA receptor NR2B to NR2A subunit switch. Neuron *70*, 339–351.

Mayor, S., Rothberg, K.G., and Maxfield, F.R. (1994). Sequestration of GPI-anchored proteins in caveolae triggered by cross-linking. Science *264*, 1948–1951.

Mikasova, L., De Rossi, P., Bouchet, D., Georges, F., Rogemond, V., Didelot, A., Meissirel, C., Honnorat, J., and Groc, L. (2012). Disrupted surface cross-talk between NMDA and Ephrin-B2 receptors in anti-NMDA encephalitis. Brain *135*, 1606–1621.

Moscato, E.H., Peng, X., Jain, A., Parsons, T.D., Dalmau, J., and Balice-Gordon, R.J. (2014). Acute mechanisms underlying antibody effects in anti-N-methyl-D-aspartate receptor encephalitis. Ann. Neurol. *76*, 108–119.

Nair, D., Hosy, E., Petersen, J.D., Constals, A., Giannone, G., Choquet, D., and Sibarita, J.-B. (2013). Super-resolution imaging reveals that AMPA receptors inside synapses are dynamically organized in nanodomains regulated by PSD95. J. Neurosci. *33*, 13204–13224.

Oddone, A., Vilanova, I.V., Tam, J., and Lakadamyali, M. (2014). Super-resolution imaging with stochastic single-molecule localization: concepts, technical developments, and biological applications. Microsc. Res. Tech. *77*, 502–509.

Paoletti, P. (2011). Molecular basis of NMDA receptor functional diversity. Eur. J. Neurosci. *33*, 1351–1365.

Pennacchietti, F., Vascon, S., Nieus, T., Rosillo, C., Das, S., Tyagarajan, S.K., Diaspro, A., Del Bue, A., Petrini, E.M., Barberis, A., and Cella Zanacchi, F. (2017). Nanoscale Molecular Reorganization of the Inhibitory Postsynaptic Density Is a Determinant of GABAergic Synaptic Potentiation. J. Neurosci. *37*, 1747–1756.

Planagumà, J., Leypoldt, F., Mannara, F., Gutiérrez-Cuesta, J., Martín-García, E., Aguilar, E., Titulaer, M.J., Petit-Pedrol, M., Jain, A., Balice-Gordon, R., et al. (2015). Human N-methyl D-aspartate receptor antibodies alter memory and behaviour in mice. Brain *138*, 94–109.

Planagumà, J., Haselmann, H., Mannara, F., Petit-Pedrol, M., Grünewald, B., Aguilar, E., Röpke, L., Martín-García, E., Titulaer, M.J., Jercog, P., et al. (2016). Ephrin-B2 prevents N-methyl-D-aspartate receptor antibody effects on memory and neuroplasticity. Ann. Neurol. *80*, 388–400.

Ricci, M.A., Manzo, C., García-Parajo, M.F., Lakadamyali, M., and Cosma, M.P. (2015). Chromatin fibers are formed by heterogeneous groups of nucleosomes *in vivo*. Cell *160*, 1145–1158.

Rust, M.J., Bates, M., and Zhuang, X. (2006). Sub-diffraction-limit imaging by stochastic optical reconstruction microscopy (STORM). Nat. Methods *3*, 793–795.

Shi, J., Aamodt, S.M., and Constantine-Paton, M. (1997). Temporal correlations between functional and molecular changes in NMDA receptors and GABA neurotransmission in the superior colliculus. J. Neurosci. *17*, 6264–6276.

Specht, C.G., Izeddin, I., Rodriguez, P.C., El Beheiry, M., Rostaing, P., Darzacq, X., Dahan, M., and Triller, A. (2013). Quantitative nanoscopy of inhibitory synapses: counting gephyrin molecules and receptor binding sites. Neuron *79*, 308–321.

Xing, G.G., Wang, R., Yang, B., and Zhang, D. (2006). Postnatal switching of NMDA receptor subunits from NR2B to NR2A in rat facial motor neurons. Eur. J. Neurosci. *24*, 2987–2992.

Zhang, Z., and Sun, Q.Q. (2011). Development of NMDA NR2 subunits and their roles in critical period maturation of neocortical GABAergic interneurons. Dev. Neurobiol. *71*, 221–245.

Cell Reports, Volume *23*

Supplemental Information

NMDA Receptor Autoantibodies in Autoimmune Encephalitis Cause a Subunit-Specific Nanoscale Redistribution of NMDA Receptors

Laurent Ladépêche, Jesús Planagumà, Shreyasi Thakur, Irina Suárez, Makoto Hara, Joseph Steven Borbely, Angel Sandoval, Lara Laparra-Cuervo, Josep Dalmau, and Melike Lakadamyali

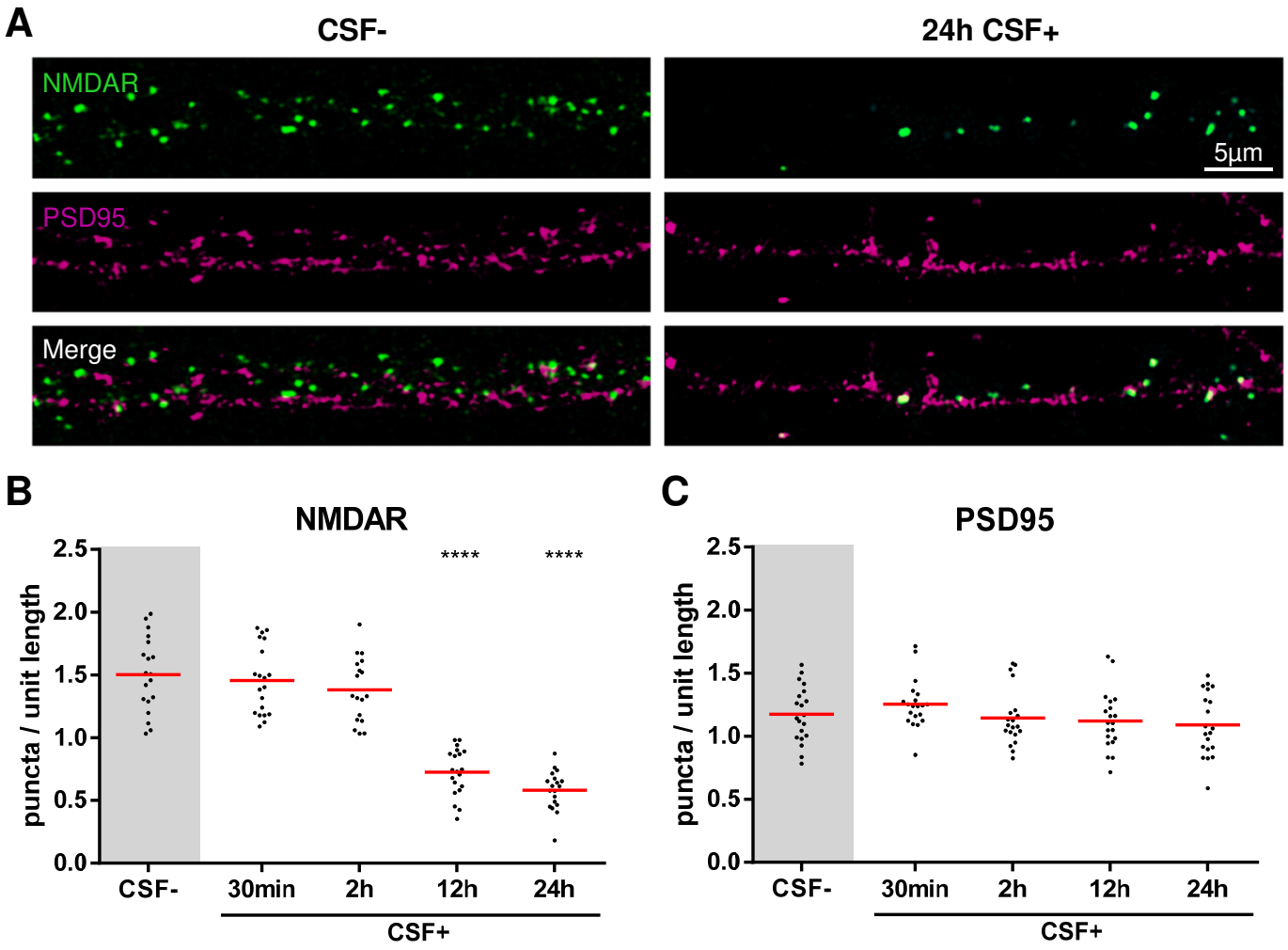

Figure S1: NMDAR autoantibodies induce a reduction in the surface density of NMDAR (related to Figure 1)

(**A**) Representative confocal images of surface NMDAR (green, upper panels) labelled together with PSD95 (magenta, middle panels) after 24 hr of incubation with control or patients' CSF (CSF-, upper panels, and CSF+, lower panels, respectively).

(**B-C**) Neurons were treated for 30 min, 2, 6, 12 or 24 hr with control or patients' CSF (CSF- and CSF+ respectively) and the number of NMDAR puncta per unit length (µm) of dendrite was measured for surface NMDAR (**B**) and PSD95 (**C**). Red lines represent means and the dots correspond to individual cells (NMDAR n = 19, 20, 18, 20 and 19 fields of view respectively, from left to right; NMDAR n = 20, 20, 20, 20 and 20 fields of view respectively, from left to right; ****$p < 0.0001$, Kruskal-Wallis test).

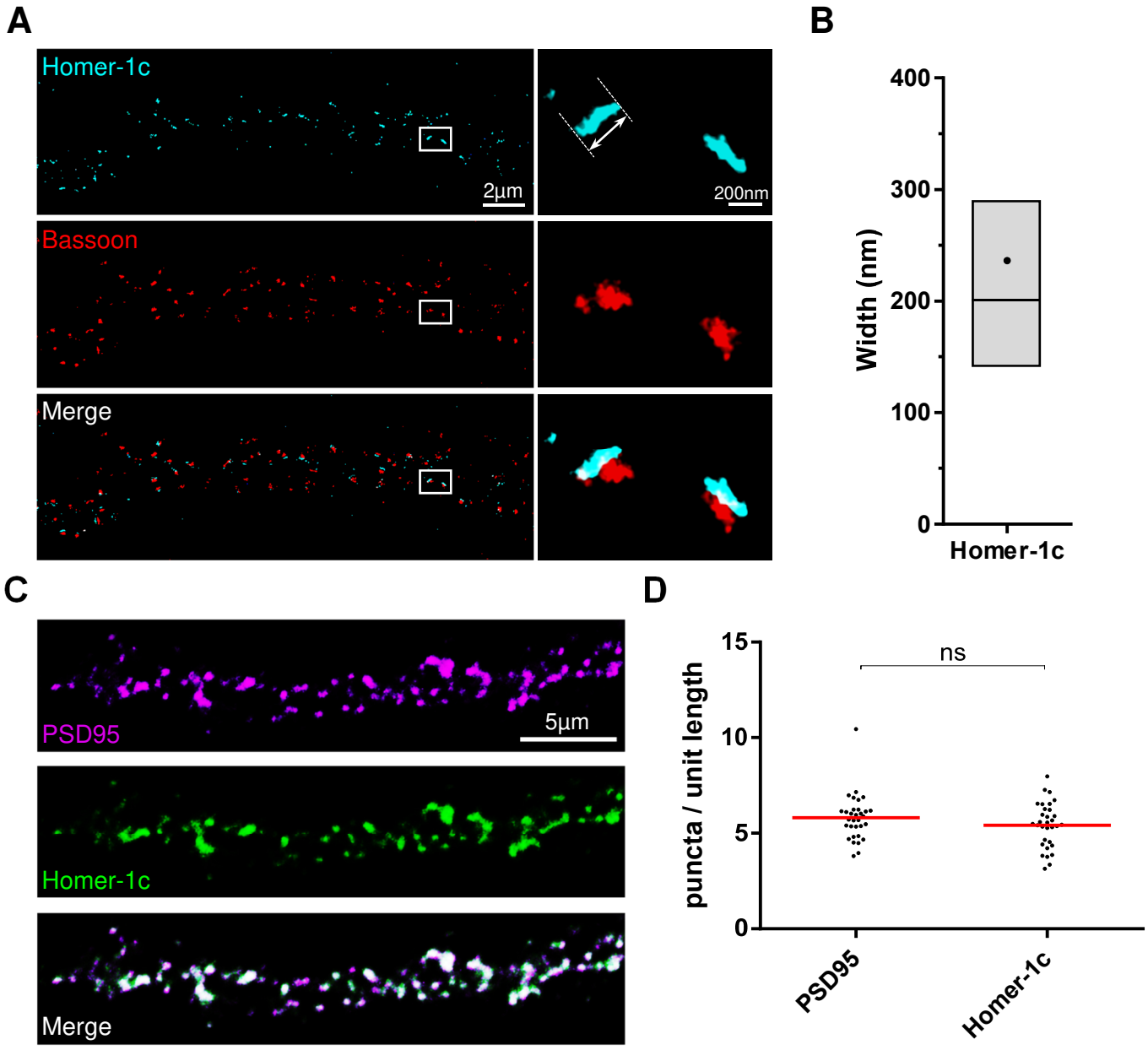

Figure S2: Imaging of the postsynaptic density protein Homer-1c as a synaptic structural reference (related to Figure 1)

(**A**) A representative STORM image of the postsynaptic protein Homer-1c (cyan, upper panels), and the presynaptic protein Bassoon (red, middle panels) allowed visualization of the synaptic complex (merge, lower panels).

(**B**) Quantification of the width of the Homer-1c as indicated by the dashed lines and arrows in A (upper panels, zoom). The box, line and dot correspond to interquartile range (IQR, 25th-75th percentile), median and mean, respectively (n = 622 synapses).

(**C**) Representative confocal images of the postsynaptic proteins PSD95 (magenta, upper panel) and Homer-1c (green, middle panels), showing a strong colocalization (white, lower panel).

(**D**) Quantification of the density of postsynaptic proteins PSD95 and Homer-1c puncta per unit length (µm) of dendrite. Red lines represent the means and dots correspond to individual cells (n = 32 and 32 fields of view respectively, from left to right; ns $p > 0.05$, Mann-Whitney test).

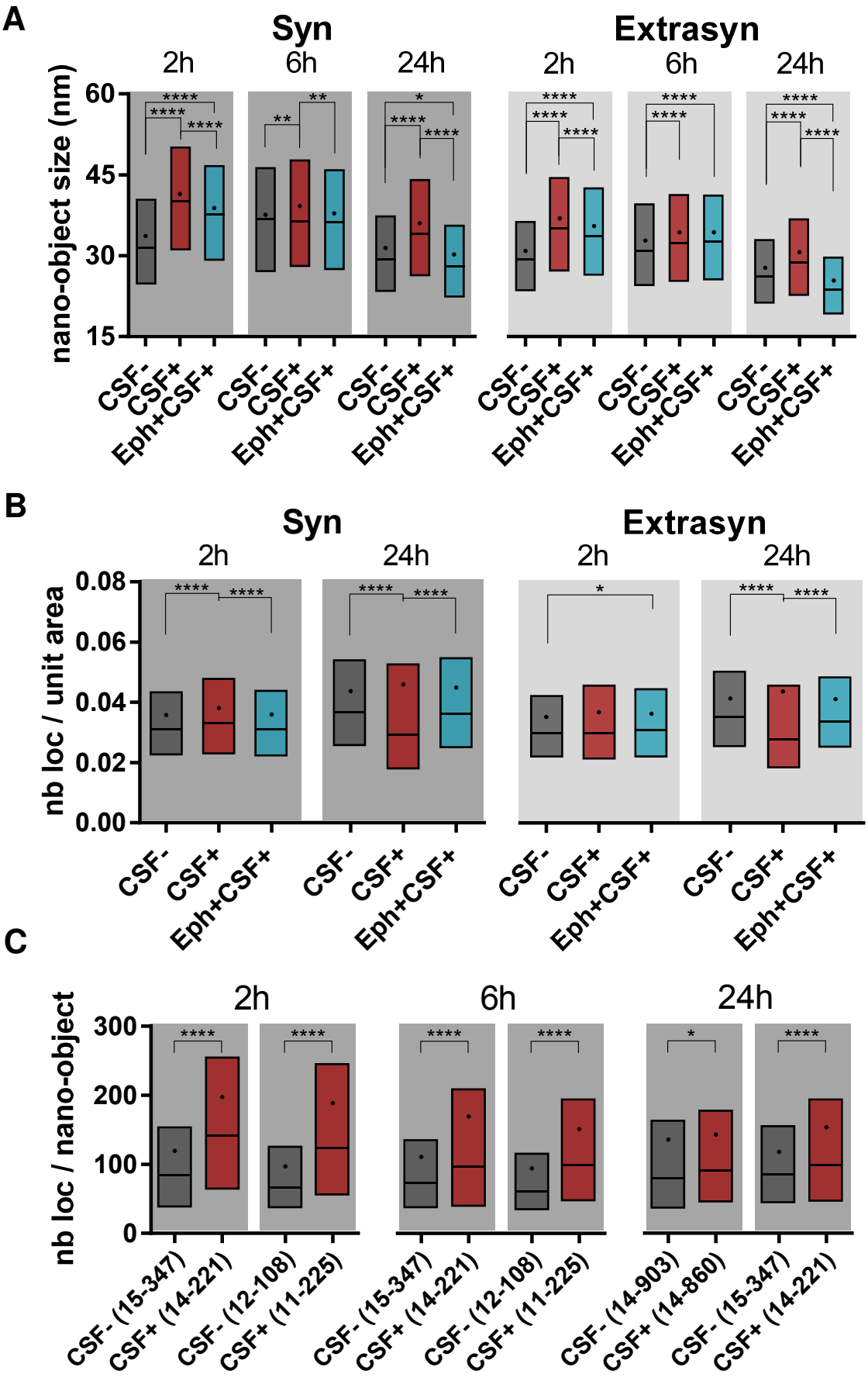
A
Syn
Extrasyn
2h
6h
24h
nano-object size (nm)
60
45
30
15
CSF-
CSF+
Eph+CSF+
B
nb loc / unit area
0.08
0.06
0.04
0.02
0.00
C
nb loc / nano-object
300
200
100
0
CSF- (15-347)
CSF+ (14-221)
CSF- (12-108)
CSF+ (11-225)
CSF- (14-903)
CSF+ (14-860)

Figure S3: NMDAR autoantibodies induce time-dependent changes in the size and receptor packing density of the NMDAR nano-objects (related to Figure 2)

Quantification of the surface NMDAR nano-object size (**A**) and localization density (number of localizations per unit nano-object area) representing the packing density of NMDARs inside nano-objects (**B**) after 2, 6 or 24 hr of incubation with the control CSF (CSF-, dark grey), the patients' CSF alone (CSF+, red) or in presence of ephrin-B2 (Eph+CSF+, cyan). The box, line and dot correspond to interquartile range (IQR, 25^{th}-75^{th} percentile), median and mean, respectively (Synaptic nano-objects size n = 3039, 4957, 4849, 5183, 5238, 4396, 2498, 3994 and 835 nano-objects respectively, from left to right; Extrasynaptic nano-objects size n = 9310, 11313, 12148, 9404, 15196, 13421, 6993, 5903 and 2001 nano-objects respectively, from left to right; Synaptic nano-objects density n = 3039, 4957, 4849, 2498, 3994 and 835 nano-objects respectively, from left to right; Extrasynaptic nano-objects size n = 9310, 11313, 12148, 6993, 5903 and 2001 nano-objects respectively, from left to right; *p < 0.05, **p < 0.01, ***p < 0.001, ****p < 0.0001, Kruskal-Wallis test).

(**C**) Inter-experiment variations in the receptor content of the NMDAR nano-objects after treatment with different batches of patients' antibodies. Quantification of the number of localizations per NMDAR nano-object after 2, 6 or 24 hr of incubation with various control (CSF-, dark grey) and patients' CSF (CSF+, red). The box, line and dot correspond to interquartile range (IQR, 25^{th}-75^{th} percentile), median and mean, respectively (n = 1045, 2033, 4560, 8810, 1733, 2390, 4279, 11899, 381, 1264, 2425, 1270 nano-objects respectively, from left to right).

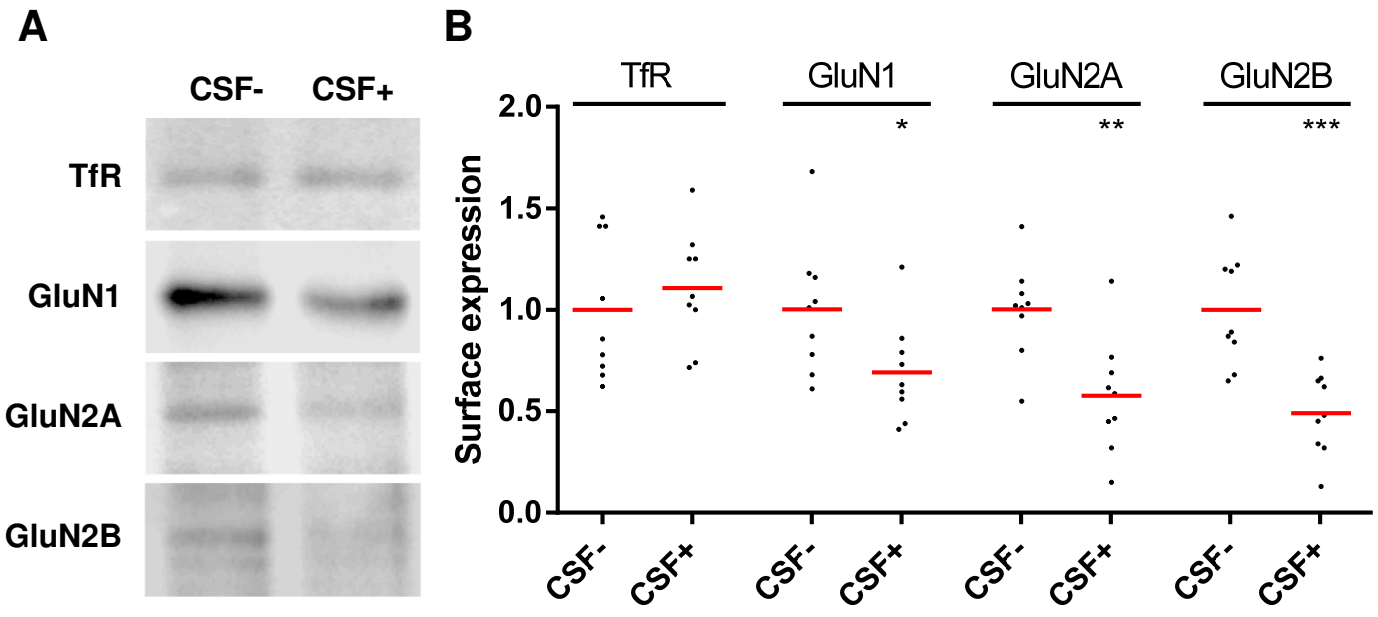

Figure S4: The protein surface levels of GluN2A- and GluN2B is reduced after 24 hr incubation with NMDAR autoantibodies (related to Figure 3)

(A) Immunoblot of biotinylated surface proteins of hippocampal neurons treated with control or patients' CSF for 24 hr. The protein bands were demonstrated using specific antibodies directed against the GluN1, GluN2A and GluN2B subunits. The transferrin receptor is used as a loading control.

(B) Quantitative densitometry analysis of the immunoblots. The data was normalized to the values of neurons treated with the control CSF. Red lines represent means and the dots correspond to individual blots (n = 9 blots for each condition; *p < 0.05, **p < 0.01, ***p < 0.001, Unpaired t-test with Welch's correction).

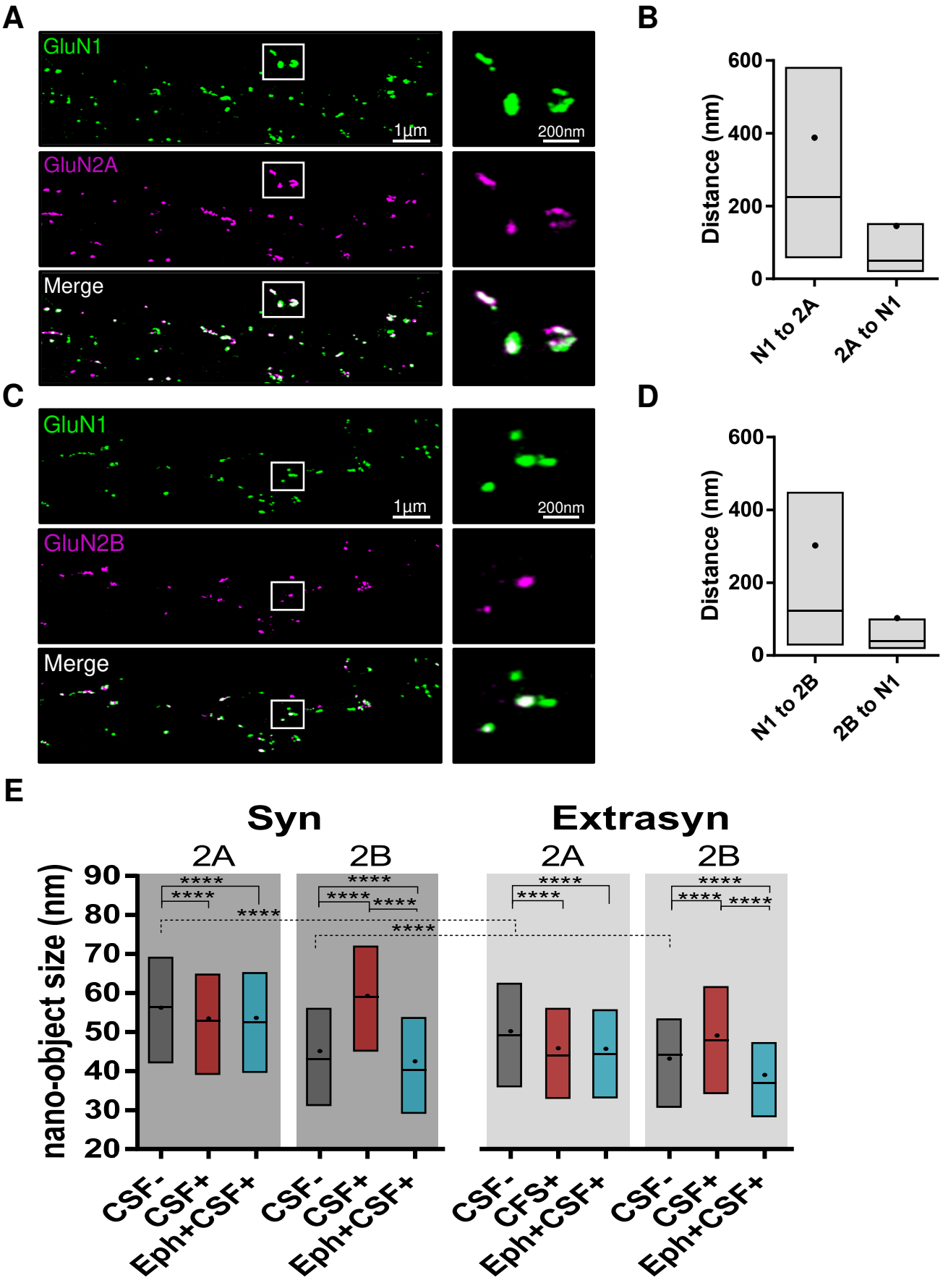
A
GluN1
1µm
200nm
GluN2A
Merge
B
Distance (nm)
600
400
200
0
N1 to 2A
2A to N1
C
GluN1
1µm
200nm
GluN2B
Merge
D
Distance (nm)
600
400
200
0
N1 to 2B
2B to N1
E
Syn
Extrasyn
2A
2B
2A
2B
nano-object size (nm)
90
80
70
60
50
40
30
20
****
CSF-
CSF+
Eph+CSF+
CFS+

Figure S5: 24 hr incubation with patients' CSF antibodies induces an increase in GluN2B-NMDAR nano-object size (related to Figure 3)

(**A, C**) Surface GluN2A and GluN2B colocalize with GluN1. Representative STORM images of GluN1 (green, upper panels) and GluN2A (**A**) or GluN2B (**C**) subunits (magenta, middle panels). Right panels display zooms of the white squared regions.

(**B, D**) Quantification of the nearest neighbor distance between the GluN1 nano-objects and the closest GluN2A/B nano-object (n = 13320 and 12722 GluN1 nano-objects respectively, from left to right), as well as the distance between the GluN2A/B nano-objects and the closest GluN1 nano-object (n = 5997 GluN2A and 7663 GluN2B nano-objects). While GluN1 is expected to be present in all NMDAR nano-objects, GluN2A and GluN2B are optional subunits that are present in a sub-population of NMDAR nano-objects. Hence, GluN1 should only partially co-localize with GluN2 whereas GluN2 should fully co-localize with GluN1, which is reflected by the much shorter distance from GluN2 to its nearest GluN1 nano-object. The box, line and dot correspond to interquartile range (IQR, 25^{th}-75^{th} percentile), median and mean, respectively.

(**E**) Quantification of the size of surface GluN2A- or GluN2B-NMDAR nano-objects after 24 hr incubation with control CSF (CSF-, dark grey), patients' CSF alone (CSF+, red) or in presence of ephrin-B2 (Eph+CSF+, cyan). The box, line and dot correspond to interquartile range (IQR, 25^{th}-75^{th} percentile), median and mean, respectively (Synaptic n = 4912, 2649, 3869, 4219, 6317 and 3162 nano-objects respectively, from left to right; Extrasynaptic n = 9312, 5213, 6395, 7938, 10086 and 7530 nano-objects respectively, from left to right; ****$p < 0.0001$, Kruskal-Wallis test for multiple comparisons and Mann-Whitney test for pair comparisons).

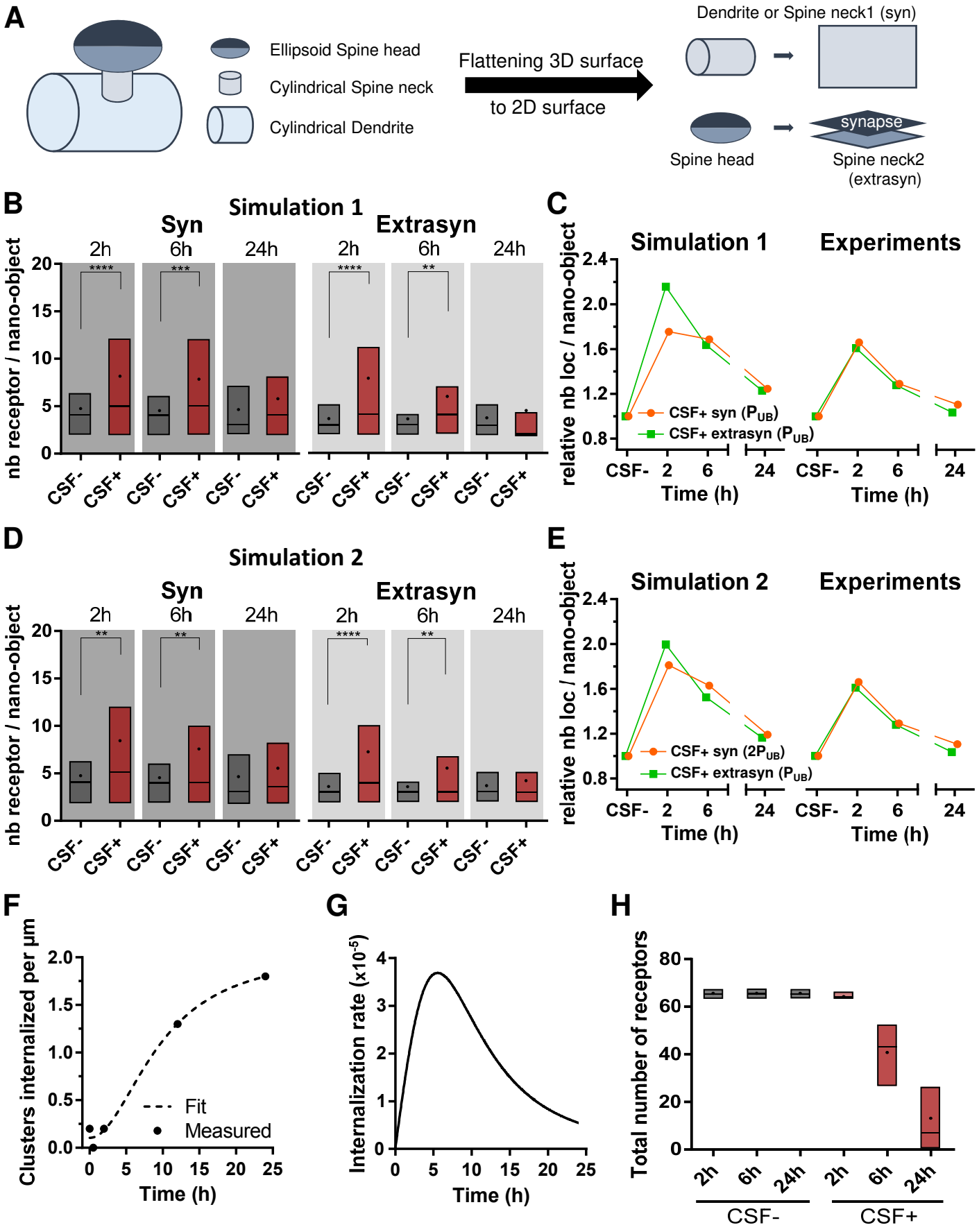
A
Ellipsoid Spine head
Cylindrical Spine neck
Cylindrical Dendrite
Flattening 3D surface
to 2D surface
Dendrite or Spine neck1 (syn)
synapse
Spine head
Spine neck2
(extrasyn)
B
Simulation 1
Syn
Extrasyn
2h
6h
24h
nb receptor / nano-object
CSF-
CSF+
C
Simulation 1
Experiments
relative nb loc / nano-object
CSF+ syn (P_UB)
CSF+ extrasyn (P_UB)
Time (h)
D
Simulation 2
E
Simulation 2
Experiments
CSF+ syn (2P_UB)
F
Clusters internalized per µm
Fit
Measured
Time (h)
G
Internalization rate (x10^-5)
H
Total number of receptors
CSF-
CSF+

Figure S6: Monte Carlo simulations suggest binding time of receptor to scaffold protein affects cluster content in synapse and extrasynapse for CSF+ (related to Figure 4)

(**A**) Schematic description of how the neuronal surface areas were generated for the simulation. Dendrite is represented by a cylinder surface, the spine consists of a cylindrical neck (spine neck1, considered extra synaptic) and an ellipsoidal spine head (bottom surface is spine neck2 considered extrasynaptic, and top surface is the synapse). Area is calculated for each of the surfaces and then flattened to a 2D surface of equivalent area.

In (**B, C**) the probability of receptor unbinding from SPR under control and antibody conditions in both extrasynapse and synapse is P_{UB}=0.167 (Synaptic n = 282, 218, 289, 158, 277 and 73 nano-objects respectively, from left to right; Extrasynaptic n = 220, 179, 222, 122, 218 and 58 nano-objects respectively, from left to right). In (**D, E**) the probability of receptor unbinding from SPR under antibody condition in extrasynapse is the same (P_{UB} =0.167), but in the synapse is $2P_{UB}$=0.333 (Synaptic n = 282, 201, 289, 141, 277 and 46 nano-objects respectively, from left to right; Extrasynaptic n = 220, 196, 222, 120, 218 and 60 nano-objects respectively, from left to right).

(**B, D**) Distribution of receptors per nano-object at 2, 6 and 24 hr time points in the synapse and extrasynapse, in both CSF- and CSF+ conditions, obtained from simulation. The box, line and dot correspond to interquartile range (IQR, 25^{th}-75^{th} percentile), median and mean, respectively, (**p < 0.01, ***p < 0.001, ****p < 0.0001, Mann-Whitney test).

(**C, E**) Comparison of the fold-change in nano-object content at different time points (2, 6 and 24 hr) relative to the corresponding CSF- values for simulations (left) and experimental data (right). Each data point is obtained by normalizing the mean of receptors per nano-object value at each time point for CSF+ with the mean of receptors per nano-object value obtained from the corresponding time points for CSF-.

(**F**) Cumulative number of internalized nano-objects per micron for CSF+ at different time points. Data points are derived from experimentally obtained number of nano-objects per micron remaining on the surface at 2, 6 and 24 hr for CSF+ (Figure 1B) and then fitted to the Logistic function y = A2 + (A1-A2)/(1 + (x/x0)^p).

(**G**) Rate of nano-object internalization derived from experimental observation. Data points are obtained by differentiating the fit representing cumulative number of internalized nano-objects per micron for CSF+ at different time points.

(**H**) Total number of receptors present on the surface of neuron at 2, 6 and 24 hr for CSF- and CSF+, obtained from simulation. The box, line and dot correspond to interquartile range (IQR, 25^{th}-75^{th} percentile), median and mean, respectively (n = 40, 40, 40, 50, 50 and 48 runs respectively, from left to right).

Table S1: List of different patient CSFs used in each experiment (related to Experimental Procedures)

Experiment	# CSF+	# CSF -
GluN1		
Confocal	11-110 & 12-053	12-266 & 13-164
STORM		
2h xp1	14-221	15-347
2h xp2	11-225	12-108
2h xp3	11-225	12-108
6h xp1	14-221	15-347
6h xp2	14-221	15-347
6h xp3	11-225	12-108
6h xp4	11-225	12-108
24h xp1	12-053	13-164
24h xp2	14-860	14-903
24h xp3	14-860	14-903
24h xp4	14-860	14-903
24h xp5	14-860	14-903
24h xp6	14-860	14-903
24h xp7	14-221	15-347
24h xp8	14-221	15-347
GluN2A-2B		
Confocal	14-221	15-347
STORM		
xp1	14-221	15-347
xp2	14-221	15-347
xp3	14-221	15-347

SUPPLEMENTAL EXPERIMENTAL PROCEDURES

Primary cultures of neurons

Briefly, primary hippocampal neurons were prepared from stage E18 embryos extracted from pregnant Wistar rats. Embryonic brains were extracted from the skull using fine forceps. Hippocampi were isolated, trypsinated in 0.20% Trypsin solution in Hanks' Balanced Salt Solution (HBSS) buffer (Sigma-Aldrich, St Louis, MO) for 15 min at 37°C, washed twice in HBSS buffer for 5min and mechanically disaggregated by pipette suction in high glucose DMEM medium (complemented with 10% Horse Serum, 10% Fetal Bovine Serum, 1% L-Glutamine, 1% Penicillin-Streptomycin and 1% Sodium Pyruvate) (Sigma-Aldrich). Neurons were plated at 120,000 cells per Corning 35 mm (P35) dishes (Sigma-Aldrich) in Neurobasal medium supplemented with B-27 Supplement (Thermo-Fisher, Waltham, MA) on poly-L-lysine-coated (Sigma-Aldrich) coverslips. Cells were maintained at 37°C, 5% CO2, 95% humidity and neurons were cultured for 16-21 days *in vitro* before use.

Animal procedures were conducted in accordance with standard ethical guidelines (European Communities Directive 86/609/EU) and approved by the local ethical committees.

CSF samples and treatments

Samples of CSF from 5 different patients with high titer of NMDAR antibodies (CSF+, determined according to previous studies, see Dalmau et al., 2008) were used on cultured neurons to determine the effects of the patients' antibodies (**Table S1**). Samples of CSF from 5 different subjects lacking antibodies that target NMDAR (CSF-) were used as controls (**Table S1**). The treatment consisted in adding 40 µl of patients' or control CSF to the cultured hippocampal neurons P35 plates containing 1 ml of Neurobasal medium supplemented with B-27 Supplement (Thermo-Fisher). At the end of the desired treatment time (depending on the experiment), cultures were washed with phosphate buffered saline (PBS). Written consent for studies was obtained from patients or from families if patients were judged unable to give consent. Studies were approved by the institutional review board of Hospital Clínic and Institut d'Investigacions Biomèdiques August Pi i Sunyer (IDIBAPS), Universitat de Barcelona.

Immunostaining for confocal microscopy

To determine the surface levels of NMDAR subunits, live neuronal cultures were incubated 1 hr at 37°C with either patients' CSF (used as an anti-GluN1 antibody, 1:200, Hospital Clínic, Barcelona), rabbit antibodies directed against surface epitopes of GluN2A (1:200, ACG-002, Alomone, Jerusalem, Israel) or GluN2B (1:200, ACG-003, Alomone). After washing with equilibrated culture medium, neurons were then incubated 30 min with either Alexa Fluor 488 goat anti-human IgG (A11013, 1:1000, Molecular Probes) or Alexa Fluor 488 goat anti-rabbit IgG (A32731, 1:1000, Molecular Probes) in equilibrated culture medium with 1% BSA for 30 min at 37°C. Cells were then fixed with PFA 4% in PBS for 10 min and then permeabilized with 0.3% v/v Triton X-100 (Sigma-Aldrich) in PBS for 10 min at room temperature, and blocked for 1 hr with 1% BSA in PBS. Cells were then incubated 1 hr at room temperature using a mouse antibody directed against PSD95 (1:200, MA1-045, Thermo-Fisher). Following the incubation with the primary antibodies, slides were washed and incubated for 1 hr at room temperature with Alexa Fluor 594 goat anti-mouse IgG

(R37121, 1:1000, Thermo-Fisher). Slides were then mounted with ProlonGold with 4′,6-Diamidino-2-phenylindole dihydrochloride (DAPI, P36935, Molecular Probes) and results scanned at 1024x1024 lateral resolution and Nyquist optimized z-sampling frequency with a confocal microscope (Zeiss LSM710) with EC-Plan NEOFLUAR CS 100x, 1.3 NA oil immersion objective. For spot analysis we performed image deconvolution using the AutoQuantX3 software (Bitplane AG, Zurich, Switzerland) followed by automatic segmentation using the spot detection algorithm from Imaris suite 7.6.4 (Bitplane). The density of spots was expressed as number of puncta per µm length of dendrite. To determine the synaptic location of GluN2 subunits, a spot co-localization algorithm between GluN2A or GluN2B and PSD95 was applied using Imaris. The same procedure was followed to compare the density of PSD95 and Homer-1c clusters. After fixation and permeabilization, cells were incubated 1 h at room temperature using a rabbit antibody directed against PSD95 (1:200, 124002, Synaptic Systems) and a guinea pig antibody against Homer-1c (1:200, 160004, Synaptic Systems). Following the incubation with the primary antibodies, slides were washed and incubated for 1 h at room temperature with Alexa Fluor 594 goat anti-rabbit IgG (R37117, 1:1000, Thermo-Fisher) and Alexa Fluor 488 goat anti-guinea pig IgG (A-11073, 1:1000, Thermo-Fisher). Slides were mounted and analyzed as described above.

Immunoblot for biotinylated cell-surface proteins

To assess the effects of patient's antibodies on cell surface levels of GluN1, GluN2A, and GluN2B NMDAR subunits, neurons were especially plated at a density of 500,000 in P35 plates and were treated with patients' or control CSF, for 24 hr. Neurons were then washed twice in cold PBS, and incubated with 1.5 $mg.ml^{-1}$ EZ Link Sulfo-NHS-LC Biotin (Thermo Fisher Scientific) in cold PBS for 30 min at 4°C. The excess of free biotin was quenched by incubating with cold PBS supplemented with 100 mM Glycine for 20 min. Neurons were then rinsed in PBS and lysated with 150 mM NaCl, 1 mM EDTA, 100 mM Tris HCl, 1% TritonX-100, 1% sodium deoxycholate, 0.1% SDS containing protease cocktail inhibitor (diluted 1:50, Sigma-Aldrich) shaking for 1 hr at 4°C. Lysates were cleared of debris by centrifugation at 13,000g for 20 min, the supernatant was collected and protein concentration measured using the bicinchoninic acid assay (PierceTM BCA Protein Assay Kit, Thermo Fisher Scientific). Equal amount of biotinylated proteins from neurons treated with either CSF (800 µg) were then incubated with avidin-linked agarose beads (PierceTM High Capacity Neutravidin Agarose, Thermo Fisher Scientific) at 4°C overnight. The beads were rinsed with 3 column volumes of PBS, and the surface fraction was eluted with 2 column volumes of SDS loading buffer. The surface fraction was then analyzed by immunoblot. For each condition, equal amounts of proteins were loaded onto 8% SDS-polyacrylamide gels and transferred to PVDF membrane. The membrane was blocked with 5% non-fat skimmed milk and incubated with the primary antibodies at 4°C overnight. The primary antibodies used for the immunoblots were: rabbit anti-GluN1 (1:1000, G8913, Sigma-Aldrich), rabbit anti-GluN2A (1:500, AGC-002, Alomone labs) or rabbit anti-GluN2B (1:500, AGC-003, Alomone labs), or mouse anti-transferrin receptors (1:2000, clone H68.4, Thermo Fisher Scientific). After incubation with primary antibodies, membranes were incubated with horseradish-peroxidase conjugated secondary antibodies (anti-rabbit IgG; 1:1000, or anti-mouse IgG; 1:10,000) for 1 hr at room temperature, and visualized with enhanced chemiluminescence (all Amersham GE Healthcare) on a LAS4000 (GE Healthcare). Protein concentrations were quantified by using scanning densitometry with Fiji ImageJ software. Surface expression of GluN1, GluN2A, and GluN2B were normalized with that of the transferrin receptor as a loading control.

STORM Imaging

Immunostaining for STORM

To determine the synaptic distribution of NMDAR subunits, after having been treated with either control or patients' CSF for 2, 6 or 24 hr, in presence or absence of ephrin-B2 (0.5µg.ml^{-1}, 50598-M08H, Sino Biological), cultured neurons were incubated live with primary antibodies in equilibrated culture medium with 1% BSA for 30 min at 37°C. Primary antibodies used for labeling before fixation for the STORM experiments were: patients' CSF (used as an anti-GluN1 antibody, 1:200, Hospital Clinic, Barcelona), rabbit antibodies anti-GluN2A (1:50, ACG-002, Alomone) or rabbit antibodies anti-GluN2B (1:50, ACG-003, Alomone). After washing with equilibrated culture medium, neurons were then incubated with the corresponding secondary donkey anti-human or anti-rabbit antibodies (1:20, Jackson ImmunoResearch) labeled with Alexa Fluor 405-Alexa Fluor 647 dye pair in equilibrated culture medium with 1% BSA for 30 min at 37°C. Cells were then fixed with PFA 4% in PBS for 10 min and then permeabilized with 0.3% v/v Triton X-100 (Sigma-Aldrich) in PBS for 10 min at room temperature, and blocked for 1 hr with 1% BSA in PBS. Followed a 1 hr incubation at room temperature with a mouse antibody anti-PSD95 (1:200, MA1-045, Thermo-Fisher) in 1% BSA in PBS and another 1 hr incubation at room temperature with a secondary donkey anti-mouse (1:20, Jackson ImmunoResearch) labelled with Cy3-Alexa Fluor 647 dye pair in 1% BSA in PBS. The same procedure was followed to visualize synaptic structure labelling Bassoon and Homer-1c. After fixation and permeabilization, cells were incubated 1 hr at room temperature using a mouse antibody directed against Bassoon (1:400, ADI-VAM-PS003, Enzo) and a guinea pig antibody against Homer-1c (1:200, 160004, Synaptic Systems). Following the incubation with the primary antibodies, slides were washed and incubated for 1 h at room temperature with the corresponding secondary donkey anti-guinea pig antibodies (1:20, Jackson ImmunoResearch) labeled with Alexa Fluor 405-Alexa Fluor 647 dye pair and a secondary donkey anti-mouse (1:20, Jackson ImmunoResearch) labelled with Cy3-Alexa Fluor 647 dye pair in equilibrated culture medium with 1% BSA for 30 min at 37°C.

For STORM imaging, the secondary antibodies were labeled in-house with different combinations of dye pairs of activator/reporter, as previously described (Bates et al., 2007). Briefly, the dyes were purchased as NHS ester derivatives: Alexa Fluor 405 Carboxylic Acid Succinimidyl Ester (Invitrogen), Cy3 mono-Reactive Dye Pack (GE HealthCare), and Alexa Fluor 647 Carboxylic Acid succinimidyl Ester (Invitrogen). Antibody labeling reactions were performed by incubating for 40 min at room temperature a mixture containing the secondary antibody, NaHCO3, and the appropriate pair of activator/reporter dyes diluted in DMSO. Purification of labeled antibodies was performed using NAP5 Columns (GE HealthCare). The dye to antibody ratio was quantified using Nanodrop and only antibodies with a composition of 3-4 Cy3 or 4.5-5 Alexa Fluor 405 and 0.8-1.2 Alexa Fluor 647 per antibody were used for imaging.

STORM Imaging

STORM combines two concepts: single molecule localization and fluorophore photoswitching. The first concept allows one to localize the position of a single fluorophore with nanometer precision. Photoswitching makes it possible to "turn off" most fluorophores into a dark state and "turn on" only a small subset of them at a time. As a result, the images of the "active" fluorophores are isolated in space and their positions can be localized with high precision. Once all the fluorophores are imaged and their positions are localized, a high-resolution image can be reconstructed from these localizations. All imaging experiments were carried out with a commercial STORM microscope system from Nikon Instruments (NSTORM). For single color imaging, 647 nm laser light was used for exciting the reporter dye (Alexa Fluor

647, Invitrogen) and switching it to the dark state, and 405 nm laser light was used for reactivating the Alexa Fluor 647 into a fluorescent state via an activator dye (Alexa Fluor 405)–facilitated manner. An imaging cycle was used in which one frame belonging to the activating light pulse (405 nm) was alternated with four frames belonging to the imaging light pulse (647 nm). Dual color imaging was performed with two sets of secondary antibodies labeled with the same reporter dye (Alexa Fluor 647) but two different activator dyes (Alexa Fluor 405 and Cy3) (Bates et al., 2007). In addition to the 405 nm laser light, an imaging cycle with 561 nm laser light as the activating light pulse was used for reactivating Alexa Fluor 647 linked to the second activator dye (Cy3).

The emitted light was collected by a 100×, 1.49 NA oil immersion objective, filtered by an emission filter (ET705/72 m), and imaged onto an electron multiplying charge coupled device (EMCCD) camera at an exposure time of 20 ms per frame.

Imaging was done using a previously described imaging buffer (Cysteamine MEA [Sigma-Aldrich, #30070-50G], Glox Solution: 0.5 $mg.ml^{-1}$ glucose oxidase, 40 $mg.ml^{-1}$ catalase [all Sigma-Aldrich], 10% Glucose in PBS) (Bates et al., 2007).

STORM Data Analysis

STORM images were analyzed and rendered as previously described (Bates et al., 2007; Huang et al., 2008b, 2008a). Briefly, peaks in single-molecule images were identified based on a threshold and fit to a simple Gaussian to determine the x and y positions. The raw STORM data consist of a list of x-y coordinates, corresponding to the localized positions of fluorophores. There is not a one-to-one relationship between the number of localizations and the number of molecules (in our case, NMDAR subunits) in STORM images mainly for three reasons: i) the antibody epitope labeling efficiency may not be 100%, ii) each antibodies can have a different number of fluorophores and, iii) each fluorophore can undergo multiple photoswitching events, resulting in multiple localizations arising from a single fluorophore.

The final images were rendered by representing each x-y position (localization) as a Gaussian with a width that corresponds to the determined localization precision (9 nm). Sample drift during acquisition was calculated and subtracted by reconstructing STORM images from subsets of frames (typically 500–1000 frames, for which drift was assumed to be small) and correlating these images to a reference frame (typically one that is reconstructed at the initial time segment).

For multicolor images, each peak was color-coded based on whether the emission was recorded immediately after 405 nm or 561 nm activation cycle. The peaks coming from a frame not belonging to the one right after an activation frame were coded as “non-specific.” A crosstalk algorithm as described previously was applied to correct for non-specific activations by the imaging laser (Dani et al., 2010). Briefly, the number of “apparent specific” activations were calculated from the frame immediately following the activation pulse and the number of “non-specific” activations from subsequent imaging frames in the imaging cycle. Assuming that the probability of “non-specific” activations is constant across all frames, we could then determine the number of “actual specific” activations by subtracting the “non-specific activation” number from the “apparent specific” activation number. We then used these numbers to statistically subtract crosstalk due to “non-specific” activations in an unbiased way as previously described (Dani et al., 2010).

Rendered images were finally processed using a previously developed algorithm (Ricci et al., 2015). Briefly, STORM data consisting in x-y localization lists were used to construct discrete localization images, such that each pixel has a

value equal to the number of localizations falling within the pixel area (pixel size = 15 nm). From the localization images, density maps were obtained by 2-dimensional convolution with a square kernel (3x3 pixels^2). A constant threshold (15 localizations) was used to digitize the density maps into binary images, such that pixels have a value of 1 where the density is larger than the threshold value and a value of 0 elsewhere. Connected components of the binary image, composed by adjacent non-zero pixels (4-connected neighbors), were sequentially singled out and analyzed. Localization coordinates within each connected component were grouped by means of a distance-based clustering algorithm. Initialization values for the number of nano-objects and the relative centroid coordinates were obtained from local maxima of the density map within the connected region, calculated by means of a peak finding routine. Localizations were associated to nano-objects based on their proximity to nano-object centroids. New nano-object centroid coordinates were iteratively calculated as the average of localization coordinates belonging to the same nano-object. The procedure was iterated until convergence of the sum of the squared distances between localizations and the associated nano-object and provided nano-object centroid positions and number of localizations per nano-object. Nano-object sizes were calculated as the SD of localization coordinates from the relative nano-object centroid.

Analyses were performed by means of custom code written in Matlab.

Monte-Carlo simulations

The dendrite was considered as a cylinder with a length of 200 nm and radius of 100 nm, which was flattened to a 2D square area of 400 nm^2. The spine was placed randomly on the dendrite which consist of a spine neck (referred as Spine neck1) represented as a cylinder and a spine head represented as an ellipsoid (**Figure S6A**). The height and radius of the neck were selected randomly from a range of 20-100 nm, which was also flattened to a rectangular 2D surface. The spine head of the spine is an ellipsoid with height, major and minor axis dimensions selected randomly from a range of 30–100 nm. Half surface area of this ellipsoid was calculated (mean value ~ .036 um^2) and compared with area of a square (~190 nm length). The total spine head surface was thus represented by two square surfaces of 190 nm length each, stacked one above the other. The top surface is the synapse, and the bottom surface belongs to extrasynapse, referred as spine neck2 (**Figure S6A**). Scaffold proteins present on the neuron surface as concentrated pockets (Nair et al., 2013) were modelled as confined regions with square geometry for simplicity (Scaffold Protein Regions, **Figure 4A**). It was observed that the fraction of the dendritic and synaptic surface area designated to the SPRs, effected the receptor dynamics under control condition. 12 SPRs of 24 nm dimension each were distributed equally over dendritic and synaptic surfaces (tuned to recapitulate receptor dynamics for control condition). The centers of 2 SPRs were separated by a minimum distance of 34 nm, again a value tuned to represent the control receptor dynamics.

Under control conditions, nano-objects were formed due to receptors binding to regions of high density scaffold proteins (represented as SPR). Fixed number of receptors were designated to each SPR providing the initial receptors per nano-object value of the dendrite and the synapse, with 1.3 times (based on experimental observation) more receptors in the synaptic SPRs. Receptors were allowed to bind to SPRs in the synapse with probability $P_B = 1$. However, in the extrasynaptic sites receptors were allowed to bind SPRs with a lower binding probability, assuming reduced presence of SPR and/or reduced NMDAR affinity for SPR (tuned to $0.6P_B$). Receptors were allowed to unbind from the SPRs with an unbinding probability $P_{UB} = 0.167$, a value that was optimized based on previous experimentally determined residence times (1-20s) of AMPA receptors inside nanodomains (Nair et al., 2013). The unbound receptors were allowed to diffuse

with a probability $P_D = 1$. Diffusion steps were drawn from a MATLAB generated normal distribution having the variance calculated from experimentally observed diffusion coefficients of NMDA receptors (median = 1 x 10^{-3} mm².s^{-1}, 25-75% = 3 x 10^{-4} - 4 x 10^{-2} mm².s^{-1}, Mikasova et al., 2012). The above mentioned probabilities along with other adjustable parameters, including receptor density (~0.2 receptors/ nm^2), number and size of SPRs (12 SPRs with 576 nm^2 of area each), and receptor diameter (5 nm) were optimized such that the receptors per nano-object remained constant over the different time points of the control simulation (**Movie S1**). In simulation 1, we considered nano-object formation whenever 2 or more receptors came into a proximity of 9 nm (distance tuned taking in consideration the approximate diameter of a receptor-antibody complex). This effect resulted in an increase of the size of existing nano-objects, and the merging and formation of new nano-objects independent of the SPRs. Receptor cross-linking also decreased the diffusion probability of any receptor out of a nano-object (value tuned to $0.05P_D$, P_D is the receptor diffusion probability under control condition.

Simulation algorithm in detail:

a) Initial distribution of the receptors on the surface

Under control conditions, nano-objects were formed due to receptors binding to regions of high density scaffold proteins (represented as SPR). At time zero, 90% of the total receptors (*nr_total* = 70) were distributed in the SPRs forming the initial nano-objects (*nr_nano-object,* number of receptors forming nano-objects) and the rest 10% was distributed randomly outside the SPR *(nr_free,* number of receptors not part of any nano-object. 20% of *nr_free* was present in the dendrite and the rest 80% present in the synapse. Fixed number of receptors (with 10% of incorporated variation) were designated to each SPR providing the initial receptors per nano-object value of the dendrite and the synapse, with 1.3 times (experimental observation) more receptors in the synaptic SPRs. We had to tune the density and distribution of the initial receptors to recapitulate receptor dynamics under control conditions. The distribution of receptors depended on the receptors per nano-object value and was calculated by

$$(Receptors\ per\ nano\text{-}object_{dend} \times no\ of\ SPR_{dend}) + (1.33 \times Receptors\ per\ nano\text{-}object_{dend} \times no\ of\ SPR_{syn}) = nr\_nano\text{-}object$$

Coordinates for the receptors were selected randomly and the minimum distance between centres of two receptors' was 2x*rad*, where *rad* is the radius of a receptor. The radius for the receptor was also tuned and was an important parameter as it effected the steric hindrance and hence their diffusion.

b) Receptor dynamics

100 ms was taken as the iteration time step (Δt). Every simulation iteration involves the following processes.

1. Internalization: The experimental data provides the number of nano-objects per micrometer remaining on the surface (nano-object density) at 2, 6 and 24 hr for CSF+ (**Figure 1B**). From the above data we could derive the number of nano-objects internalized per micron at different time points (by subtracting the maximum value from the data set) and fit it with the Logistic function (**Figure S6F**):

$$y = A2 + (A1-A2)/(1 + (x/x0)^p)$$

By differentiating the fitted function, we obtained the rate of internalization of nano-objects for every 100 ms (**Figure S6G**). The density of nano-objects assumed for the simulation is 4 times more than experimental observation (**Figure**

1B). Therefore, the rate of internalization observed experimentally, was scaled by a factor of 4 to obtain the probability of internalization:

$$4 \text{ x } Internalization\ rate(t)_{experimental}\ x\ \Delta t.$$

Every iteration was checked for internalization of nano-objects with the calculated probability. If internalization occurred, then an existing nano-object from the dendrite was randomly selected and all the receptors comprising that nano-object was made unavailable for any further processes.

2. Diffusion: Every unbound receptor was visited in each iteration and checked for diffusion with $P_D = 1\Delta t$ (all the receptors for CSF- condition; and only receptors not part of nano-object for CSF+ condition) and $P_D = 0.05\Delta t$ (Receptors part of nano-object for CSF+ condition). Diffusion steps were drawn from a MATLAB generated normal distribution having the variance calculated from experimentally observed diffusion coefficients of NMDA receptors (Mikasova et al., 2012).

Evaluating steric effect of a diffusing receptor

If a receptor *r1*, was selected to diffuse by a step $d1 = x1 + y1$, then it can only diffuse if there is no other receptor *r2* placed at an angle θ (relative to *r1*) and at a distance less than *d1*. In case there is a receptor *r2*, *r1* will diffuse only till the boundary of receptor *r2*. *r2* and *r1* are then iterated over all the receptors respectively.

3. Boundary conditions: The boundary conditions were applied to the edges of the dendrite, neck1, neck2 and synapse surfaces. Conditions were applied so that receptors have continuity of motion over these surfaces.

4. Update receptor states after diffusion: All the receptors were updated in every iteration, after diffusion. Under control condition nano-objects were formed only in the SPRs. Therefore, after diffusion receptor position was checked and if found to be present inside SPR, it was considered part of that existing nano-object. Similarly, a receptor that diffused out of SPR, was considered a free receptor. Under antibody condition, if a diffused receptor was found to be within a distance of 9 nm from a second receptor, it was considered part of existing nano-object the second receptor belonged to. In case the second receptor was a free receptor, a new nano-object was created. All nano-objects had a number assigned to them and receptors were indexed for the nano-objects they belonged to. Nano-object numbers and receptor indexes were updated if two or more nano-objects merged into one; or a new nano-object number was assigned in case a new nano-object formed. Nano-object numbers and receptor index information was required for nano-object internalization process. Lastly, it was checked, if any diffused receptor had its position in the SPR.

5. Binding and unbinding dynamics of receptors: Every receptor was visited to check for binding and unbinding events in case they were positioned inside SPRs. Synaptic receptors bound to SPR with a probability $P_B = 1x\Delta t$ and extrasynaptic receptors with $P_B = 0.6x\Delta t$ under control conditions. The synaptic receptors were considered to bind SPR with almost certainty while the binding probability for the extrasynaptic receptors was tuned to represent the control condition receptor dynamics. Both synaptic and extrasynaptic receptors unbound from the SPR with a probability $P_{UB} = (1/6)x\Delta t$ under control conditions. P_{UB} was calculated considering 6 s as the residence time constant of the NMDAR in the SPR. The time constant was tuned from a range of 1-20s of residence times of AMPAR inside nanoclusters, observed experimentally (Nair et al., 2013). In case of antibody condition, the unbinding probabilities had to be increased in a differentiated manner for the extrasynaptic ($1.5P_{UB}$) and the synaptic ($2P_{UB}$) receptors but was implemented after 1.5 hr. The receptors in this case had unbinding probabilities similar to control simulation till 1.5 hr was reached.

6. Nano-object evaluation: At the end of every time point, the nano-objects and receptors per nano-objects were recalculated, assuming any two receptors as part of a nano-object if they were separated by 15 nm (experimental resolution).

7. Data analysis: The distribution of 'Receptors per nano-object' was calculated from all the nano-objects in the synapse/extrasynapse identified from 50 simulations (~200 nano objects). The distribution of 'Total number of receptors' present on the surface was obtained by counting the total receptors (within and outside of a nano object in synapse/extrasynapse) after every simulation. In some simulations at 24 hr time point, there were 0 receptors present both in the synapse and extrasynapse. We did not include these results in the statistics which reduced the overall N < 50.

Videos recapitulating the simulations results were made using the image processing toolbox Dip-image for Matlab (Hendriks et al., 1999).

Results of Simulations 1 and 2

Simulation 1: To capture the receptor dynamics in the presence of patients' NMDAR antibodies, we took into account the occurrence of antibody-induced cross-linking by allowing nano-object formation whenever 2 or more receptors came into proximity decided by their radii Second, we implemented internalization of extrasynaptic nano-objects with a rate determined from the experimental data (**Figure S5F-H**). These two effects only partially recapitulated the experimentally observed changes to NMDAR nano-objects in the presence of patients' antibodies (**Figure S6B and S6C**). With this simulation, the number of NMDARs inside the nano-objects initially increased and then decreased, similar to what was observed in the experiments. However, at the 6 hr time point, there was still significant clustering of synaptic NMDARs above levels observed in the control simulation, contrary to experimental data. In addition, the extrasynaptic clustering was substantially higher than the synaptic clustering, which is opposed to the experimental results. Therefore, antibody-induced cross-linking and internalization alone could not fully capture the experimental results.

Simulation 2: Based on previous reports (Mikasova et al., 2012; Planagumà et al., 2016) and our own data showing that activation of EphB2 antagonizes the effects of the antibodies, we hypothesized that the binding of antibodies to NMDAR leads to a disruption of its interaction with EphB2 and possibly other synaptic interacting partners. We thus increased by two-fold the unbinding rate of synaptic receptors from the SPR reflecting a potential disruption of receptor-protein interactions (see Supplemantal Experimental Procedures). This modification could recapitulate better the experimental observations at the synaptic level but the amount of extrasynaptic NMDAR clustering remained inappropriately high compared with that of the synaptic NMDAR clustering (**Figure S6D and S6E**).

SUPPLEMENTAL REFERENCES

Bates, M., Huang, B., Dempsey, G.T., Zhuang, X., and Dempsey, T. (2007). Multicolor Super-Resolution Imaging with Photo-Switchable Probes Fluorescent. Science (80-.). *317*, 1749–1753.

Dalmau, J., Gleichman, A.J., Hughes, E.G., Rossi, J.E., Peng, X., Lai, M., Dessain, S.K., Rosenfeld, M.R., Balice-Gordon, R., and Lynch, D.R. (2008). Anti-NMDA-receptor encephalitis: case series and analysis of the effects of antibodies. Lancet Neurol. *7*, 1091–1098.

Dani, A., Huang, B., Bergan, J., Dulac, C., and Zhuang, X. (2010). Superresolution Imaging of Chemical Synapses in the Brain. Neuron *68*, 843–856.

Hendriks, C.L.L., van Vliet, L.J., Rieger, B., van Kempen, G.M.P., and van Ginkel, M. (1999). Dipimage: a scientific

image processing toolbox for MATLAB. Quant. Imaging Group, Fac. Appl. Sci. Delft Univ. Technol. Delft, Netherlands.

Huang, B., Wang, W., Bates, M., and Zhuang, X. (2008b). Three-Dimensional Super-Resolution Reconstruction Microscopy. 810–814.

Huang, B., Jones, S.A., Brandenburg, B., and Zhuang, X. (2008a). Whole-cell 3D STORM reveals interactions between cellular structures with nanometer-scale resolution. Nat. Methods *5*, 1047–1052.

Mikasova, L., De Rossi, P., Bouchet, D., Georges, F., Rogemond, V., Didelot, A., Meissirel, C., Honnorat, J., and Groc, L. (2012). Disrupted surface cross-talk between NMDA and Ephrin-B2 receptors in anti-NMDA encephalitis. Brain *135*, 1606–1621.

Nair, D., Hosy, E., Petersen, J.D., Constals, A., Giannone, G., Choquet, D., and Sibarita, J.-B. (2013). Super-resolution imaging reveals that AMPA receptors inside synapses are dynamically organized in nanodomains regulated by PSD95. J. Neurosci. *33*, 13204–13224.

Planagumà, J., Haselmann, H., Mannara, F., Petit-Pedrol, M., Grünewald, B., Aguilar, E., Röpke, L., Martín-García, E., Titulaer, M.J., Jercog, P., et al. (2016). Ephrin-B2 prevents N-methyl-D-aspartate receptor antibody effects on memory and neuroplasticity. Ann. Neurol. *80*, 388–400.

Ricci, M.A., Manzo, C., García-Parajo, M.F., Lakadamyali, M., and Cosma, M.P. (2015). Chromatin fibers are formed by heterogeneous groups of nucleosomes in vivo. Cell *160*, 1145–1158.